

On effective resolution in ocean models



Yves Soufflet^{a,*}, Patrick Marchesiello^a, Florian Lemarié^b, Julien Jouanno^a, Xavier Capet^c, Laurent Debreu^b, Rachid Benshila^d

^aIRD/LEGOS, 14 av. Edouard Belin, 31400 Toulouse, France

^bINRIA/LJK, 51 rue des Mathématiques, 38041 Grenoble, France

^cCNRS/LOCEAN, 4, place Jussieu, 75252 Paris, France

^dCNRS/LEGOS, 14 av. Edouard Belin, 31400 Toulouse, France

ARTICLE INFO

Article history:

Received 7 April 2015

Revised 11 December 2015

Accepted 21 December 2015

Available online 30 December 2015

Keywords:

Effective resolution

Spectral budget

Baroclinic jet

Numerical dissipation

ABSTRACT

The increase of model resolution naturally leads to the representation of a wider energy spectrum. As a result, in recent years, the understanding of oceanic submesoscale dynamics has significantly improved. However, dissipation in submesoscale models remains dominated by numerical constraints rather than physical ones. Effective resolution is limited by the numerical dissipation range, which is a function of the model numerical filters (assuming that dispersive numerical modes are efficiently removed). We present a Baroclinic jet test case set in a zonally reentrant channel that provides a controllable test of a model capacity at resolving submesoscale dynamics. We compare simulations from two models, ROMS and NEMO, at different mesh sizes (from 20 to 2 km). Through a spectral decomposition of kinetic energy and its budget terms, we identify the characteristics of numerical dissipation and effective resolution. It shows that numerical dissipation appears in different parts of a model, especially in spatial advection-diffusion schemes for momentum equations (KE dissipation) and tracer equations (APE dissipation) and in the time stepping algorithms. Effective resolution, defined by scale-selective dissipation, is inadequate to qualify traditional ocean models with low-order spatial and temporal filters, even at high grid resolution. High-order methods are better suited to the concept and probably unavoidable. Fourth-order filters are suited only for grid resolutions less than a few kilometers and momentum advection schemes of even higher-order may be justified. The upgrade of time stepping algorithms (from filtered Leapfrog), a cumbersome task in a model, appears critical from our results, not just as a matter of model solution quality but also of computational efficiency (extended stability range of predictor-corrector schemes). Effective resolution is also shaken by the need for non scale-selective barotropic mode filters and requires carefully addressing the issue of mode splitting errors. Possibly the most surprising result is that submesoscale energy production is largely affected by spurious diapycnal mixing (APE dissipation). This result justifies renewed efforts in reducing tracer mixing errors and poses again the question of how much vertical diffusion is at work in the real ocean.

© 2016 Elsevier Ltd. All rights reserved.

1. Introduction

The mesoscale ocean dynamics have been intensively studied with both observations and numerical models. Recently, the increase of numerical resolution has naturally led to the representation of a wider energy spectrum in numerical solutions (Klein et al., 2008; Capet et al., 2008b). The increase of resolution toward the kilometer scale also leads to flatter kinetic energy (KE)

spectra near the surface than those expected from interior quasi-geostrophic (QG) mesoscale dynamics with KE injection being initiated by mesoscale straining and reinforced by submesoscale turbulence. Advection then plays an important role by fluxing KE energy upward from mesoscale to large scale (inverse cascade) and downward to submesoscale (forward cascade). Consequently, part of the kinetic energy released from available potential energy (APE) leaks toward smaller scales, en route to dissipation (Molemaker et al., 2010).

The forward cascade at submesoscale implies that numerical closure (dissipation needed to remove numerical dispersive modes) can be made more consistent with physical closure. Nevertheless, dissipation in submesoscale models remains dominated by numerical constraints rather than physical ones. Model convergence at

* Corresponding author. Tel.: +33 5 61 33 29 30.

E-mail addresses: Yves.Soufflet@legos.obs-mip.fr (Y. Soufflet), Patrick.Marchesiello@ird.fr (P. Marchesiello), Florian.Lemarie@inria.fr (F. Lemarié), Julien.Jouanno@ird.fr (J. Jouanno), xclod@locean-ipsl.upmc.fr (X. Capet), Laurent.Debreu@inria.fr (L. Debreu), benshila@legos.obs-mip.fr (R. Benshila).

submesoscale is controlled by numerical dissipation, which overpowers submesoscale energy production and transfer. A misconception in submesoscale ocean modeling would be to consider that there is an intrinsic value of grid spacing that any model can use to resolve the submesoscale range (1 km or 2 km is often assumed). First, there is a strong latitudinal influence on the meso- and submesoscale ranges of the spectral energy cascade (Marchesiello et al., 2011). Second, a notion of effective resolution is needed as an indicator of the numerical dissipation range.

The concept of effective resolution is attached to that of discretization error. It is known for decades that different methods affect differently the quality of a numerical solution when using computational grids with the same resolution. Accuracy estimation in idealized problems is usually based on truncation error analysis using Taylor series expansion while dissipation and dispersion properties can be estimated from Fourier analysis (linear dispersion relation analysis). Traditionally also, pseudo-spectral models are used as calibration to assess finite difference methods (e.g., Orszag, 1971). The effective resolution can then be defined as the maximum wavenumber at which simulated waves do not deviate from some ideal solution by some prescribed relative error margin (e.g., Kent et al., 2014).

In complex oceanic and atmospheric dynamical problems, ideal solutions are difficult to find and other benchmarks must be proposed. The idea of relying on the statistical spectral characteristics of the atmospheric circulation was proposed by Skamarock (2004). In this case, a robust $-5/3$ slope of kinetic energy wavenumber spectrum is observed in the mesoscale atmospheric range, which serves as reference to the numerical model. A similarly robust statistical equilibrium is now shown to exist in many parts of the surface ocean, with a -2 spectral slope¹ in the submesoscale range, reflecting the ubiquity of surface fronts and submesoscale turbulence (Blumen, 1978; Capet et al., 2008a; 2008d; Roulet et al., 2012; and Callies and Ferrari, 2013, for a review). Effective resolution can then be defined as the dissipation wavelength below which the model kinetic energy departs from the assumed regime. This dissipation range is a function of the model's numerical filters. Inherited from the concept of scale-selective dissipation in turbulent studies (Frisch et al., 2008), it is generally believed that hyperdiffusion operators only affect the smallest scales of the spectrum, leading to an exponential decrease of kinetic energy within a finite dissipation range. We will show that this is not always true and, consequently, the concept of effective resolution must be taken with caution in oceanic and atmospheric modeling.

In this study, we assume that numerical closure is satisfied, i.e., there is enough numerical dissipation to remove numerical dispersive modes. Linear analyses show that numerical errors can be separated into two main classes, dissipative or dispersive, according to the properties of their leading term. Upwind-biased advection schemes are an example of methods that can easily be made dominantly dissipative (Shchepetkin and McWilliams, 1998; Webb et al., 1998). We will restrict ourselves to this class of methods so that the comparison between model and theoretical energy spectra is unbiased by the production of spurious energy.

Baroclinic jets have been idealized at various occasions (e.g., McWilliams and Chow, 1981) to study the generation of baroclinic instability and associated mesoscale and submesoscale dynamics. Here, we use a zonally reentrant channel where the density field is relaxed to a state that ensures distinct interior and surface insta-

¹ Frontogenesis driven by Surface-QG dynamics lead to a $k^{-5/3}$ kinetic energy spectrum in the submesoscale range (Blumen, 1978; Capet et al., 2008a). In Primitive Equations, supporting ageostrophic advection and surface instabilities, a slightly steeper $\sim k^{-2}$ spectrum is obtained (Roulet et al., 2012; Callies and Ferrari, 2013). Boyd (1992) also noted that a k^{-2} spectrum is a random discontinuity spectrum, i.e., it may express geometrical besides dynamical properties of a frontogenetic flow.

Table 1

Summary of algorithmic choices used for the various simulations presented in the paper. Acronyms are: LF = Leapfrog, HARM = Harmonic averaging, FCT = Flux Corrected Transport, FB = Forward Backward, AM3 = 3rd-order Adams-Moulton, Gen. = Generalized, RA = Robert-Asselin time filter.

Target applications	ROMS-AGRIF Regional/mesoscale	NEMO Global/climate
Horizontal grid	C	C
Vertical coordinate	Generalized σ	Partial steps
Vertical advection		
Momentum	4th-order compact	2nd-order centered w/FCT
Tracers	4th-order centered w/HARM	2nd-order centered w/FCT
Horizontal advection		
Momentum	3rd-order upwind	Split 3rd-order upwind
Tracers	3rd-order upwind	Split 3rd-order upwind
2D/3D coupling		
Free-surface	Split-explicit	Split-explicit
Temporal averaging	Power-law filter over $\frac{3}{2}\Delta t$	Flat averaging over $2\Delta t$
Time stepping		
Internal waves	LF-AM3 w/FB feedback	LF w/RA
3D momenta/tracers	LF-AM3	LF w/RA
Barotropic mode	Gen. FB	LF w/RA

stabilities. It provides a controllable test to identify the model's effective resolution of submesoscale dynamics. Our method of identifying the characteristics of turbulence cascade, numerical dissipation and effective resolution mostly relies on spectral decomposition of the energy balance, following Capet et al. (2008d) and Marchesiello et al. (2011). This method is described in Section 2, along with a presentation of the numerical models, their discretization techniques and the Baroclinic jet test case. Before analyzing the effect of numerical dissipation on effective resolution, we briefly report on the submesoscale activity generated in the test case (Section 3). Numerical dissipation is present in various parts of an ocean model and are addressed here in separate sections: spatial advection-diffusion schemes for momentum equations (KE dissipation; Section 4) and density equation (APE dissipation; Section 5), time stepping schemes (also for momentum and density) and time filters for 2D/3D mode coupling (Section 6).

2. Methods

In this section, we first describe the Regional Oceanic Modeling System (ROMS), which is used in following sections to study the effect of advection-diffusion schemes for momentum (Section 4) and density (Section 5). We also introduce the Nucleus for European Modeling of the Ocean (NEMO), which is compared with ROMS in Section 6 to discuss the effect of time discretization methods. The test case setup and diagnostics tools are also presented in this section.

2.1. ROMS

ROMS (Shchepetkin and McWilliams, 2005) is a regional model designed for simulating high resolution offshore and nearshore dynamics. ROMS is used here in its AGRIF version (see Shchepetkin and McWilliams, 2009, for a comprehensive comparison of various ROMS kernels). The different algorithmic choices relevant for the current study are summarized in Table 1. ROMS is a split-explicit, free-surface and terrain-following vertical coordinate oceanic model discretized on a C-grid. The time-stepping algorithm is third-order accurate for the integration of advective terms and second-order accurate for internal gravity waves. It is a Leapfrog Adams-Moulton predictor-corrector scheme (LF-AM3) complemented with a forward-backward feedback to extend the range of stability for internal gravity waves. The barotropic mode is integrated with a generalized forward-backward (FB) scheme

(AB3-AM4: a three-time Adams-Bashforth-like step for free-surface and a four-time Adams-Moulton-like step for velocities), which is third-order accurate. Advective terms for tracers and momentum in the horizontal are discretized using third-order upwind horizontal advection schemes (referred to as UP3). Alternatively for tracers, a better control of diapycnal mixing errors is provided by the Rotated Split UP3 (RSUP3) scheme (Marchesiello et al., 2009; Lemarié et al., 2012) and will be tested here. RSUP3 takes advantage of the natural split of upwind schemes into purely advective and diffusive parts (Webb et al., 1998; Holland et al., 1998) and rotates the latter in the isopycnal direction. For the same argument of minimizing spurious diapycnal mixing, vertical advection is discretized with high-order schemes.

2.2. NEMO

NEMO (Madec, 2008) is a state-of-the-art global model widely used in the climate community. NEMO is discretized on a C-grid with a leapfrog (LF) temporal scheme combined with a modified Robert-Asselin (RA) time filtering (Leclair and Madec, 2009) to control a spurious computational mode. Initially built with low-order discretization based on energy and enstrophy conservation principles, NEMO now offers several options for the numerical treatment of advective terms and barotropic/baroclinic mode splitting². The choices for the present study are presented in Table 1. Horizontal advection is formally discretized as in ROMS, but as the leapfrog scheme is unstable for diffusive terms, the upwind scheme is implemented with the splitting method of Webb et al. (1998) and Holland et al. (1998): centered advection is integrated with leapfrog and diffusion with a Euler forward scheme over $2\Delta t$ (Δt is model time step). The resulting scheme is referred to as split UP3 (SUP3). Vertical advection for tracers and momentum is done with a simple second-order discretization combined with a one-dimensional Flux Corrected Transport algorithm (FCT, Zalesak, 1979) to prevent numerical oscillations³. Finally, the barotropic mode is integrated as the baroclinic mode with the leapfrog time-stepping.

2.3. Stability ranges and computational cost

Stability constraints for ROMS and NEMO are given in Lemarié et al. (2015). For the numerical choices presented in Table 1, the Courant-Friedrichs-Lewy (CFL) stability constraints are respectively $\alpha_{adv}^{roms} = 1.00^4$ and $\alpha_{adv}^{nemo} = 0.50$ for advection and $\alpha_{igw}^{roms} = 0.80$ and $\alpha_{igw}^{nemo} = 0.46$ for internal gravity wave propagation⁵ (with the RA filter parameter $\nu = 0.1$). For the external (barotropic)

² The most standard option to handle the barotropic mode in NEMO makes use of a filtered free-surface scheme: an explicit filter, which has the form of an extra term in the barotropic momentum equation, is applied to slow down gravity waves while attempting to preserve slower external modes.

³ To avoid numerical instability, the first-order upstream scheme providing the monotone low-order flux in the FCT procedure is advanced using a forward Euler scheme over $2\Delta t$; the high-order scheme can be safely used with Leapfrog (e.g. Madec, 2008, Section 5.1.3).

⁴ The reduction in stability range of LF-AM3 combined with UP3 vs. C4 advection can be mitigated by using C4 during predictor and UP3 during corrector (standard choice in ROMS-AGRIF). This leads to an improvement of α_{adv}^{roms} by about 15% (from 0.86 to 1.00) without causing any adverse effects. In the split RSUP3 scheme, C4 is applied during both predictor and corrector steps and diffusion is applied separately using a Euler forward step (e.g., Marchesiello et al., 2009). In this case, α_{adv}^{roms} is slightly increased to 1.02.

⁵ In global applications, NEMO generally applies a procedure consisting of time-averaging the pressure gradient (Brown and Campana, 1978) to increase its permissible time step, provided that stability is limited by internal gravity waves. If this technique is useful to reduce computational costs in climate studies, it is probably inappropriate for submesoscale simulations because: (i) the method is less efficient as advection becomes more limiting for stability (e.g., strong vertical advection in the presence of steep topography in so-called “hot spots”; Lemarié et al., 2015); and

mode, $\alpha_{ext}^{roms} = 1.8$ and $\alpha_{ext}^{nemo} = 1$. The difference in stability constraints explain the difference in time-step limitation between ROMS and NEMO (Table 1). These numbers emphasize that high-order numerical schemes do not necessarily come at a higher computational cost because of their larger stability range.

To be more specific, we benchmarked⁶ ROMS and NEMO on the Baroclinic jet test case (described in the next section). With the present choice of numerical methods, ROMS is systematically about twice faster than NEMO in completing the simulation, despite extra-cost of a two-stage time stepping. This number may be surprising but can be understood in the light of algorithmic arguments and code profiling. First, the extended range of stability of the predictor-corrector method for the internal mode largely compensates for added computation. LF forces the computation of diffusive terms at a different time level than purely advective terms and requires a costly split of UP3 (the extra biharmonic terms for momentum components and density doubles UP3 cost). In addition, even though LF-AM3 requires two evaluations of the right hand side at each time step, costly terms like vertical and lateral diffusion are computed only once. Then, the generalized FB external mode time stepping doubles the LF range at no extra cost: the fast mode, which represents about 25% of the total cost, is twice cheaper with the generalized FB. Finally, the fast mode filtering, required in the 2D/3D coupling procedure (see Section 6.3), is 50% cheaper in ROMS because of its power-law distribution that needs a shorter time integration window than the more traditional flat-weight filter.

2.4. The Baroclinic jet test case

A semi-idealized configuration in a periodic channel is set up to generate two dominant mechanisms of upper ocean turbulence: (i) surface density stirring by mesoscale eddies and (ii) fine scale instabilities directly energizing the submesoscale range. A particular example of the latter is the Charney instability (Charney, 1947) whose relevance to the ocean is discussed in Capet et al. (2014). The baroclinic jet configuration used in this study is derived from that of Klein et al. (2008) and Roulet et al. (2012). The setup consists of a flat reentrant channel of 500 km by 2000 km by 4000 m, centered around 30 deg of latitude on a β -plane (the Coriolis frequency is 1.10^{-4} s^{-1} at the center, $\beta = 1.6 \cdot 10^{-11} \text{ m}^{-1} \text{ s}^{-1}$). Eastern/western boundary conditions are periodic while northern/southern conditions are closed. The model active tracer is potential density. The initial density field is constructed with interior and surface meridional density gradients (Fig. 1 and Appendix A for details) and associated geostrophic currents that are linearly unstable to both interior baroclinic and Charney instability modes. A linear stability analysis provides the exponential growth rate of unstable modes as a function of wavenumber (Fig. 2). The two most unstable modes are clearly distinct in length scales on either side of the Rossby deformation radius (~ 30 km in the center ± 5 km from south to north). The interior geostrophic instability thus injects energy at mesoscale and Charney instability at submesoscale.

Initial zonal velocities are in geostrophic balance with the zonally invariant density field. The level of no motion is set at the bottom, which specifies the total transport (barotropic flow).

(ii) the method sets the advection Courant number closer to its limit, which has a degrading effect on accuracy (see Section 6).

⁶ Benchmarking was performed on a linux cluster (Bull computer, Intel MPI, Processors Sandy Bridge-EP E5-2670 at 2.6 GHz, 16 cores per nodes). Both codes were compiled with “ifort -O3 -xHost -r8 -fno-alias”; the last option is to improve vectorization with pointers in NEMO. Our results were robust for all resolutions and with various choices of compiler options and parallelization. I/O operations were excluded from the computation and code profiling was performed to make sure that code performances were not accidentally spoiled by a “ballast” piece.

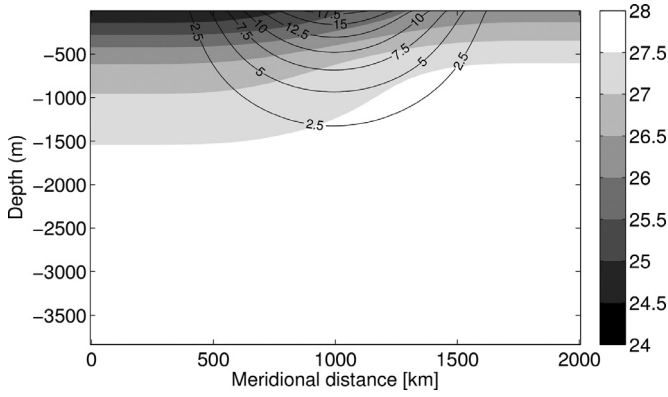


Fig. 1. Initial conditions for the Baroclinic jet test case: meridional and vertical section of density (kg/m^3 ; gray) and zonal velocity (cm/s ; isocontours).

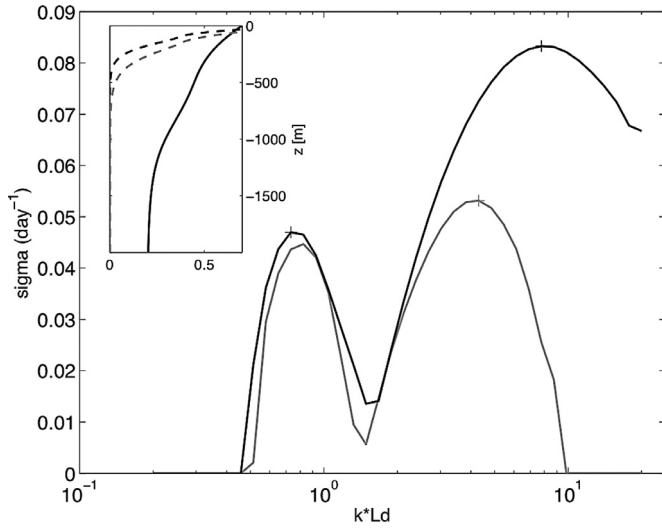


Fig. 2. Exponential growth rate of an infinitesimal perturbation of the baroclinic jet as a function of its wavenumber. Maxima are shown with a plus sign (+) for the two most unstable modes, corresponding to the interior baroclinic instability (for length-scales longer than the Rossby deformation radius) and Charney instability (for shorter scales). The black line is obtained for the baroclinic jet used as ROMS initial state (which is also the restoring state). The gray line is computed using a 20-year mean of ROMS high-resolution solutions rather than its initial state. The inset shows modulus profiles of eigenvectors of the two most unstable modes, plotted between -2000 depth and the surface. Note the surface trapping of Charney instability (dashed lines: black/gray for initial/mean state).

The jet destabilization is triggered by a very small random density perturbation. Quasi-equilibrium is then maintained by using a relaxation of the zonally averaged velocity and density fields to a basic state that corresponds to the unperturbed initial state. Density relaxation supplies the available potential energy reservoir of the solution, while flow relaxation maintains the zonal transport. In the relaxation procedure, the zonal mean state is recomputed only every ten time steps to limit computational cost but the restoring force is applied at every step to each variable ϕ :

$$\phi(x, y, z, t) \leftarrow \phi(x, y, z, t) + \frac{\Delta t}{\tau} [\bar{\phi}_0^x(y, z) - \bar{\phi}^x(y, z, t)] \quad (1)$$

where $\bar{\phi}^x$ represents the zonal mean value, ϕ_0 the initial field and τ a restoring time scale set at 50 days. τ was chosen so that the restoring force can maintain the zonal flow structure without affecting the mesoscale and submesoscale dynamics arising from it. The stability analysis performed with the initial conditions was repeated with ROMS mean state from a 20-year high-resolution simulation (Fig. 2). It confirms that the mesoscale instability and fine-

scale Charney modes are preserved by the restoring force (note however the reduction of maximum growth rates due to eddy adjustment of the initial flow).

Bottom friction follows a linear relation with coefficient $r = 5.10^{-3}$ m/s. The vertical diffusion for density and momentum use a Richardson formulation with minimum coefficients $K_T = 10^{-5}$ m²/s and $K_V = 10^{-4}$ m²/s respectively.

The test case was run for 20 years at four different horizontal resolutions: 20 km, 10 km, 5 km and 2 km, the vertical resolution is respectively 40, 60, 80 and 100 levels, with refinement in the top 100 meters of the domain (at 2 km resolution, vertical grid spacing ranges from 3 m near the surface to 200 m near the bottom). The ratio $\frac{\Delta t}{\Delta x}$ is held constant to maintain a uniform Courant number throughout the resolutions. At 2 km resolution, ROMS baroclinic time step is 320 s, giving a Courant number for internal waves about 10% lower than the maximum value $\alpha_{\text{igw}}^{\text{ROMS}} = 0.8$. In NEMO, the time step is 180 s, consistent with its lower stability range since $\alpha_{\text{igw}}^{\text{nemo}} = 0.46$.

2.5. Diagnostics: spectral KE budget

The horizontal Kinetic Energy balance for the primitive equations is:

$$\frac{1}{2} \frac{\partial u_h^2}{\partial t} = -u_h \cdot (u_h \cdot \nabla_h) u_h - u_h \cdot w \frac{\partial u_h}{\partial z} - \frac{1}{\rho_0} u_h \cdot \nabla_h p + u_h \cdot D_h + u_h \cdot \frac{\partial K_V \frac{\partial u_h}{\partial z}}{\partial z} \quad (2)$$

The rhs terms, respectively, are horizontal and vertical advective energy flux divergences, horizontal pressure work, horizontal mixing implying energy dissipation (left unspecified for now), and vertical mixing.

Following Capet et al. (2008d) and Marchesiello et al. (2011), we perform a spectral decomposition of Eq. (2) with respect to horizontal wavenumber. Averaging in time over the 20-year simulation, and in the vertical between a level z_0 and the free surface ξ gives:

$$T = \frac{1}{\xi - z_0} \int_{z_0}^{\xi} \times \Re e \left[\underbrace{-\hat{u}_h^* \cdot (\hat{u}_h \cdot \nabla) u_h}_{A_H} - \underbrace{\hat{u}_h^* \cdot w \frac{\partial u_h}{\partial z}}_{A_V} - \underbrace{\frac{1}{\rho_0} \hat{u}_h^* \cdot \nabla_h p}_{P_H} + \underbrace{\hat{u}_h^* \cdot D_h}_{D_H} + \underbrace{\hat{u}_h^* \cdot \frac{\partial K_V \frac{\partial u_h}{\partial z}}{\partial z}}_{D_V} \right] \quad (3)$$

T is the time tendency term supposed small over 20 years. The hat notation represents the Fourier transform of a variable, the caret * its conjugate, $\Re e$ the real part of the complex number and the overbar an average in time. Dropping the integral notation for simplicity and rewriting the horizontal pressure work as the sum of 3D pressure work and KE injection (i.e., buoyancy flux, with buoyancy $b = -\frac{g\rho}{\rho_0}$, supporting conversion from potential to kinetic energy), the spectral KE budget is expressed as:

$$T(k) = A_H(k) + A_V(k) + D_H(k) + D_V(k) + P(k) + I(k) \quad (4)$$

A , D , P , and I are respectively the horizontal/vertical advection, horizontal/vertical subgrid-scale mixing, pressure and injection terms:

$$A(k) = A_H(k) + A_V(k) = \Re e \left[-\hat{u}_h^* \cdot (\hat{u}_h \cdot \nabla) u_h - \hat{u}_h^* \cdot w \frac{\partial u_h}{\partial z} \right] \quad (5)$$

$$D_H(k) = A_H^{\text{UP3}} - A_H \quad (6)$$

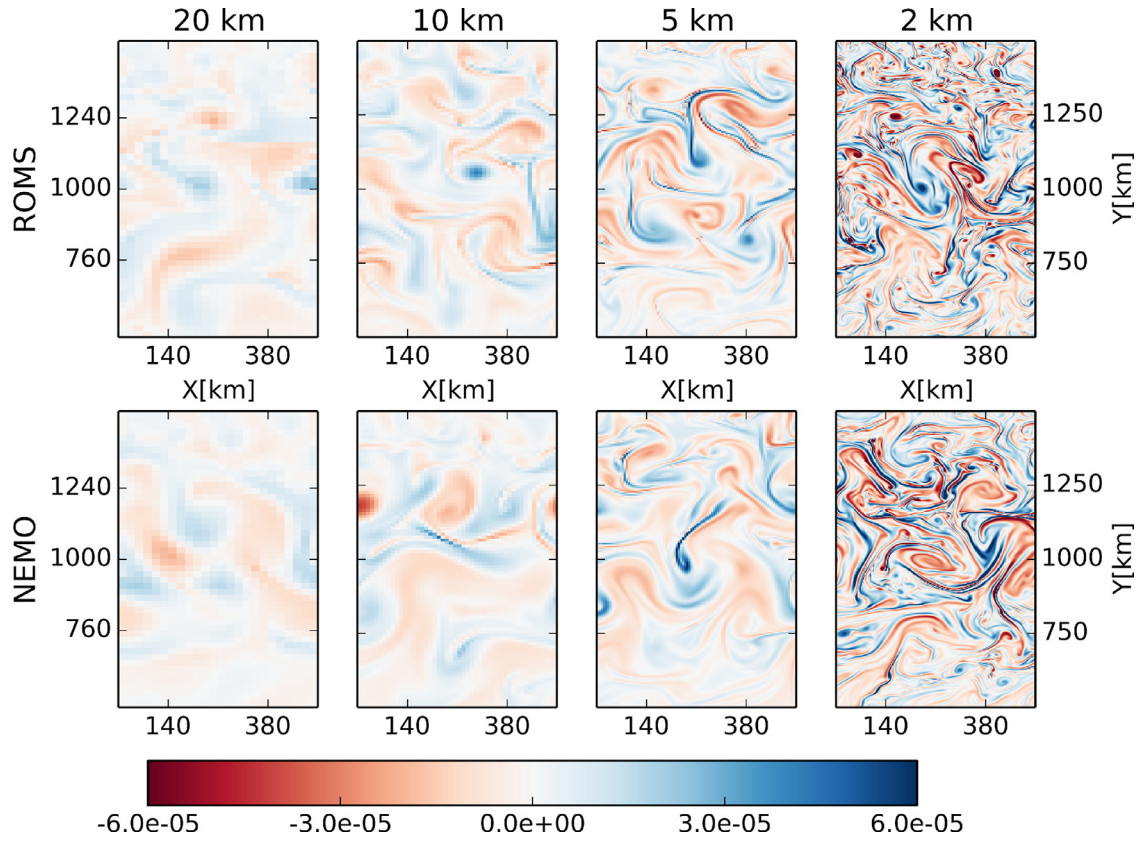


Fig. 3. Near surface relative vorticity (s^{-1}) for ROMS (top) and NEMO (bottom) at 20 km, 10 km, 5 km and 2 km resolution (from left to right). Note that only half of the meridional domain is presented (from 500 to 1500 km).

$$D_V(k) = \Re e \left[\widehat{u}_h^* \cdot \frac{\partial K_V}{\partial z} \frac{\partial \widehat{u}_h}{\partial z} \right] \quad (7)$$

$$P(k) = \Re e \left[\frac{-1}{\rho_0} \widehat{u}^* \cdot \nabla p \right] \quad (8)$$

$$I(k) = \Re e[\widehat{w}^* \widehat{b}] \quad (9)$$

$$P_H(k) = P(k) + I(k) \quad (10)$$

As noted above, the third-order upwind momentum advection scheme can be split into a non-dissipative, fourth-order, centered scheme and biharmonic dissipation term with velocity-dependent hyperviscosity. Therefore, the lateral mixing term D_H is the difference between advection terms A_H^{UP3} and A_H , computed respectively by the upwind and centered discretization schemes.

The advection term accounts for both spectral energy transfer and energy flux through the domain. The integrated lateral flux cancels out in a periodic channel and the vertical flux is small. Therefore, the advection term essentially produces spectral transfers of energy across scales. The energy transfer rate in k space (or spectral energy flux), $\Pi(k)$, can be computed as the integral in k of the advection term, assuming the flux vanishes at the highest wavenumber k_{max} (Capet et al., 2008d):

$$\Pi(k) = \int_k^{k_{max}} A dk \quad (11)$$

3. Preliminary description of submesoscale dynamics

To assess the capacity of current numerical methods to model baroclinic instabilities and associated submesoscale structures, we first look at ROMS solutions: horizontal and vertical dynamical fields, kinetic energy spectra and sources of KE in spectral space.

3.1. Horizontal structure

The upper panel of Fig. 3 represents a snapshot of ROMS surface vorticity at the four different resolutions. Increasing resolution in the model naturally leads to a broader range of scales being represented. Mesoscale structures are apparent at low resolution (20 km and 10 km) with differences in the size of fronts. As the resolution is increased, frontogenesis is more active and submesoscale structures more apparent with peak vorticity in the vicinity of fronts. At the highest resolution (2 km), turbulence is more fully developed. Numerous small scale eddies and meanders appear, which split, break or distort fronts and sometimes merge into larger eddies.

3.2. Vertical structure

The vertical profiles of Eddy Kinetic Energy (EKE; Fig. 4), show that energy increases steadily from 1500 to 500 m depth and then exponentially toward the surface. Finer resolution produces larger EKE, especially above 200 m depth where mean currents are strongest and the influence of the surface mode should be important.

The variability of vertical velocity ($w_{RMS} = \sqrt{\overline{w'^2}}$) shows a steady increase with resolution from 20 km to 5 km with a maximum around 1000 m depth; then at 2 km resolution this increase is more intense and a second peak of w_{RMS} appears near the surface, consistent with stronger vorticity fronts and submesoscale eddies. There is no sign of resolution convergence on w_{RMS} , even at mid-depth. According to Klein et al. (2008), the large increase of w variance between 5 km and 2 km resolution is due to frontal dynamics (frontogenesis and Charney instability) that affect the vertical velocity field over the whole water column.

The average profiles of buoyancy flux $\overline{w'b'}$ allows a clearer distinction between instability processes. This term represents the

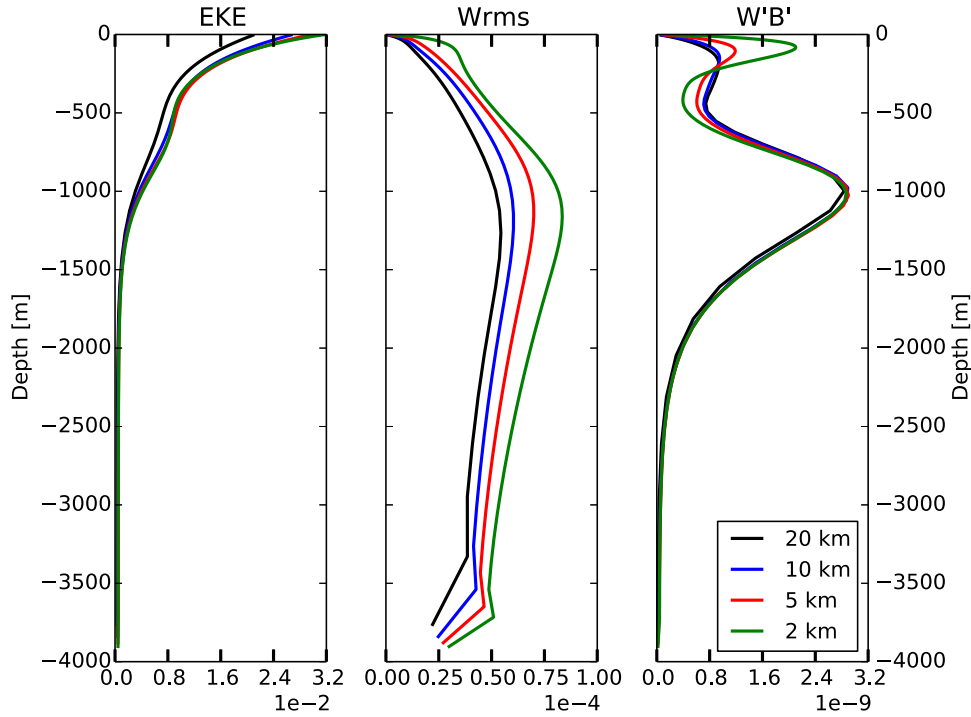


Fig. 4. ROMS vertical profiles of 20-year mean eddy kinetic energy EKE (m^2/s^2), RMS vertical velocity $w_{RMS} = \sqrt{\overline{w'^2}}$ (m^2/s^2) and eddy buoyancy flux $\overline{w'b'}$ (m^2/s^3) at 20 km, 10 km, 5 km and 2 km resolution.

conversion of available potential energy (APE) into kinetic energy, i.e., EKE production by baroclinic instability. A maximum is reached at each resolution around 1000 m depth (where the interior potential vorticity gradient changes sign) and corresponds to mesoscale production from interior baroclinic instability. Few differences appear at mid-depth between all simulations, which suggest that mesoscale KE input is well represented at all resolutions. The near surface is different: starting from 5 km resolution and most noticeably at 2 km the profiles show a large redistribution of $\overline{w'b'}$ from the subsurface (around 500 m) to the near surface. Resolution convergence thus seems to be reached for mesoscale processes associated with the interior baroclinic instability, but frontal processes have only kicked in at the highest model resolution. Anticipating on the remainder of the study we mention that the strong resolution sensitivity of the upper ocean dynamics around $\Delta x = 2$ km is inherently linked to the effect dissipation has on key submesoscale structures. In this submesoscale permitting regime we expect strong sensitivities to the numerical methods.

3.3. KE injection

The spectral budget presented in Eq. (4) is now used to evaluate the source and sink terms contribution to the near surface kinetic energy balance ($z_0 = 10$ m). If advection and pressure terms are important at large scale (not shown here), injection and dissipation become major players at submesoscale and represent the main source and sink of kinetic energy.

The near surface injection of energy in k space is presented in Fig. 5. We see a main peak at mesoscale and for the highest resolutions (5 km and 2 km) a secondary peak arising at submesoscale. The limited amount of mesoscale events even in 20 years of simulation limits the statistical reliability of the mesoscale peak and therefore the comparison between simulations. However, differences in submesoscale KE injection values are statistically robust as submesoscale events are an order of magnitude more numerous (this was confirmed by estimation of confidence intervals; not shown). Their change with resolution shows a regime transi-

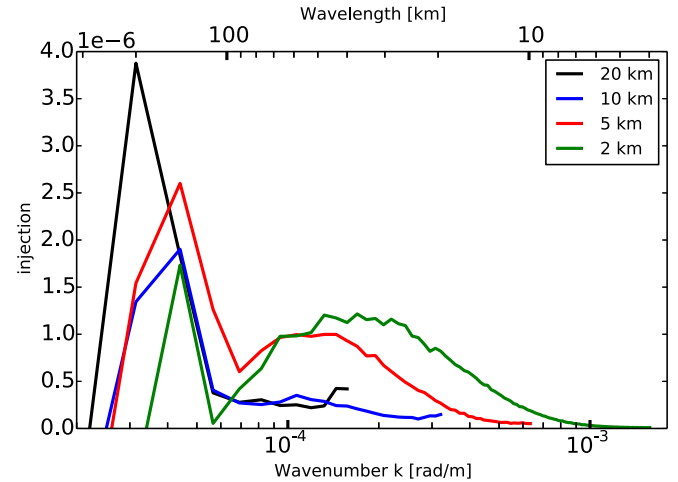


Fig. 5. ROMS near surface KE Injection spectra (m^3/s^3) at 20 km, 10 km, 5 km and 2 km resolution.

tion from coarse resolution to 5 km and finer where submesoscale injection arises. The extended range of submesoscale energy production at 2 km resolution is explained by the emergence of submesoscale instabilities (and associated frontogenesis) in addition to mesoscale driven frontogenesis (Capet et al., 2008c).

4. KE dissipation: spatial filters

In this section, we first proceed to a linear analysis of the third-order upwind advection scheme (UP3), then use it to interpret the KE and KE dissipation spectra obtained from the Baroclinic test case.

4.1. Linear analysis of hyper-dissipation

For simplicity, we consider the one-dimensional advection equation with constant velocity c_0 discretized on a grid with

regular mesh size Δx . If we note u_i the approximation of u at location $i\Delta x$, the UP3 scheme can be written:

$$c_0 \frac{\partial u_i}{\partial x} \Big|_{\text{UP3}} = \frac{c_0}{12\Delta x} \left[(-u_{i+2} + 8u_{i+1} - 8u_{i-1} + u_{i-2}) + \frac{|c_0|}{c_0} (u_{i+2} - 4u_{i+1} + 6u_i - 4u_{i-1} + u_{i-2}) \right]. \quad (12)$$

The third-order upwind scheme in Eq. (12) corresponds to the sum of a fourth-order centered approximation and a filter with coefficient $-\frac{|c_0|\Delta x}{12}$ or equivalently a biharmonic operator with hyper-diffusivity $\nu_4 = -\frac{|c_0|\Delta x^3}{12}$ scaling with local velocity and mesh size. The biharmonic diffusion term provides the leading order truncation error as shown by a Taylor expansion for $\Delta x \rightarrow 0$ that gives the modified equation:

$$\frac{\partial u}{\partial t} + c_0 \frac{\partial u}{\partial x} \Big|_{\text{UP3}} = \frac{\partial u}{\partial t} + c_0 \frac{\partial u}{\partial x} + \underbrace{\frac{|c_0|\Delta x^3}{12} \frac{\partial^4 u}{\partial x^4} - \frac{c_0\Delta x^4}{30} \frac{\partial^5 u}{\partial x^5}}_{\text{truncation error}} + \mathcal{O}(\Delta x^5).$$

If we note ω the frequency and k the wavenumber in x -direction, a Fourier transform on the discretized equation provides the dispersion relation:

$$\omega(k) = \frac{c_0}{3\Delta x} \left\{ \frac{8 \sin k\Delta x - \sin 2k\Delta x}{2} - i \frac{|c_0|}{c_0} (1 - \cos k\Delta x)^2 \right\} \quad (13)$$

$$\approx k c_0 \left[1 - \frac{(k\Delta x)^4}{30} \right] - ik|c_0| \frac{(k\Delta x)^3}{12} \quad \text{for well resolved waves} \quad (14)$$

The real part of ω represents the dispersive error of UP3, which is identical to that of a fourth-order centered scheme. The imaginary part of ω is the damping factor indicating the amplitude error, i.e., the dissipation needed to control numerical dispersion. Although we have not seen it done before in the literature, we found that the damping factor $\Im(\omega)$ can be expressed in terms of group velocity error. The exact group velocity for the advection equation is c_0 while the numerical group velocity c_g for the fourth-order centered scheme is:

$$c_g = \frac{d\Re(\omega)}{dk} = c_0 \left(\frac{4}{3} \cos k\Delta x - \frac{1}{3} \cos 2k\Delta x \right). \quad (15)$$

Combining Eqs. (14) and (15), it can easily be shown that $\Im(\omega)$ is a linear function of the group speed error, i.e., a measure of the dispersive error:

$$\Im(\omega) = -2 \left[\frac{c_0 - c_g(k)}{(n+1)\Delta x} \right], \quad (16)$$

n is the order of the scheme ($n=3$ for UP3). In Appendix B, we show that this relation holds for any linear upwind advection scheme, i.e., for any odd value of n . Eq. (16) simply states that upwind schemes are naturally designed to effectively damp their dispersive error at each wavenumber k (that of the centered scheme of order $n+1$). This is illustrated in Fig. 6 showing the normalized damping factor and group velocity curves as a function of wavenumber and wavelength in units of Δx . The figure also clearly shows that damping in the third-order scheme is small only for scales larger than $10\Delta x$ ($50\Delta x$ for the first-order scheme). Finally, note that for well resolved waves:

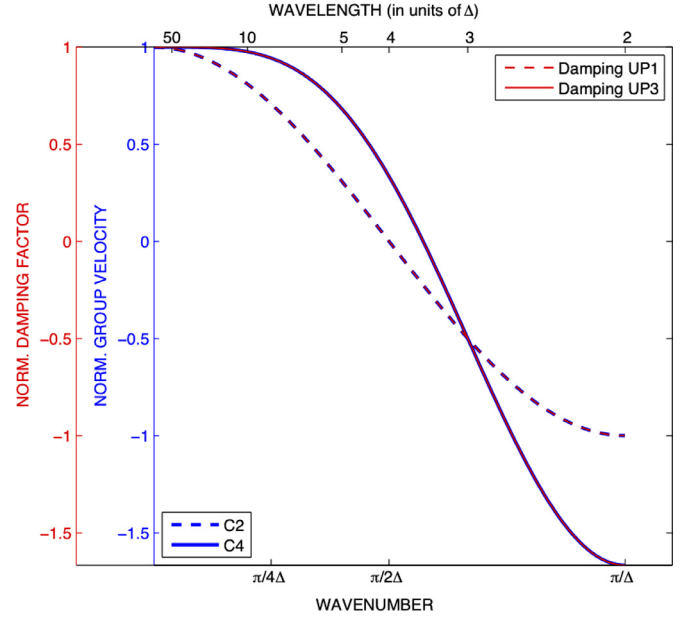


Fig. 6. Normalized damping factor and group velocity as a function of wavenumber (bottom) and wavelength (top) in units of Δx for the first (UP1) and third-order (UP3) upwind advection schemes.

$$\Im(\omega) \approx -\frac{|c_0|\Delta x^3}{12} k^4 = \nu_4 k^4 \quad (17)$$

Therefore, hyper-dissipation is expected to follow a k^4 relationship for scales larger than the grid scale, which is the expected behavior of the non-discretized biharmonic operator in k space. Near the grid size, the variation with k slows down (see Fig. 6) due to numerical approximations. In the case of the full model equations, the model kinetic energy is no longer constant in k space and dissipation $\nu_4 k^4 E(k)$ becomes dependent on the spectral kinetic energy distribution $E(k)$.

4.2. KE spectrum

The surface kinetic energy spectra at different resolution are shown in Fig. 7 in log scale. They are calculated from 5-day instantaneous output, integrated over the first 10 m depth and averaged over the 20-year simulation. The largest scale (and lowest wavenumber) represented in the spectra is half the domain width (250 km). At this scale all resolutions agree on the level of kinetic energy, although the log scale masks some random differences due, in part at least, to insufficient sampling of the mesoscale events. The smallest length scale represented in the spectra is $2\Delta x$, a function of grid resolution. At submesoscale, the density of kinetic energy is very sensitive to resolution and increases with it. At 2 km resolution, the spectrum rolls off as k^{-2} , i.e., with a gentle slope that reflects the ubiquity of surface fronts generated by mesoscale stirring and submesoscale turbulence (e.g., Callies and Ferrari, 2013). At this resolution (and to a lesser extent at 5 km), the dissipation range (exponential tail of the spectra) seems clearly separated from the submesoscale range (the center part of the spectra). The scale separating the two regimes is the effective resolution of the model according to Skamarock (2004). Here, effective resolution is only clearly defined for the 2 km resolution model and is around 20 km, i.e., $10\Delta x$. The 5 km resolution simulation is a transitional case that will be useful in our sensitivity tests for emphasizing numerical effects on the submesoscale range. For coarser resolutions, KE spectra have no distinct slopes for the submesoscale and dissipation ranges that can help identify their effective resolution.

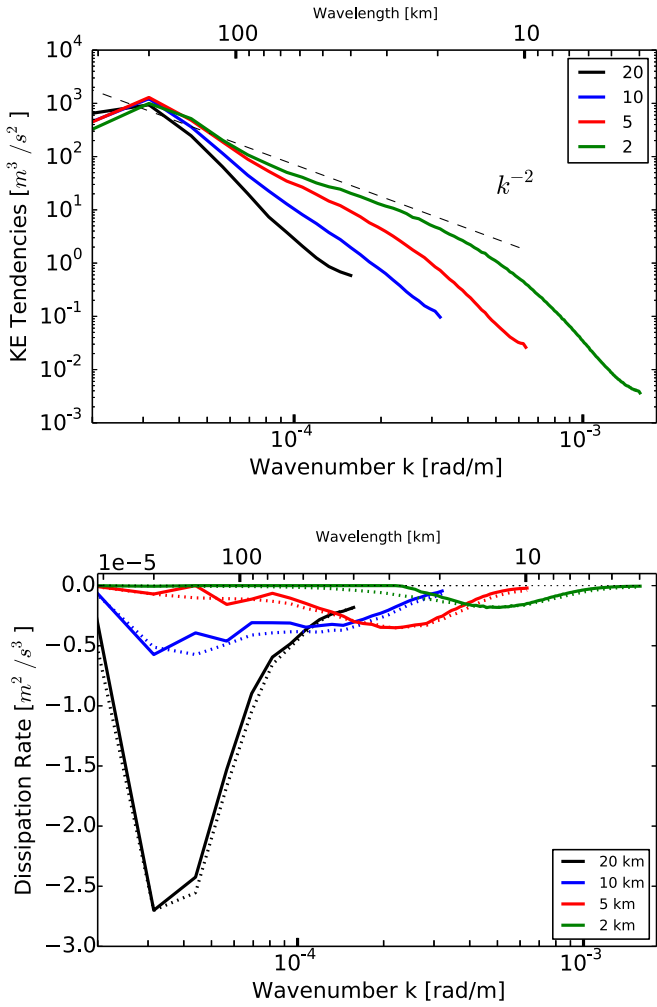


Fig. 7. Top panel: ROMS near surface KE spectra (m^3/s^2) at 20 km, 10 km, 5 km and 2 km resolution, averaged over 20 years of simulation. Bottom panel: associated near surface KE dissipation spectra (m^2/s^3). In dotted lines, reconstructed KE dissipation spectra from the theoretical damping factor: $D_H^0 = \Im(\omega)E(k) = -\frac{\partial \epsilon}{\partial x} (1 - \cos k\Delta x)^2 E(k) \sim \nu_4 k^4 E(k)$, to be compared with the original term D_H ; c_0 is taken here as the model mean velocity. Note that the approximation $D_H^0 \sim \nu_4 k^4 E(k)$ gives a result (not shown) close to the non-approximated relation for well-resolved waves, i.e., at scales larger than $3\Delta x$.

4.3. KE dissipation

Fig. 7 (bottom panel) shows that the spectral dissipation term D_H follows a bell-shaped function. At 2 km resolution, the bell-shape is well defined and dissipation is confined to wavelength between the grid size and less than 30 km. This allows the submesoscale range to develop at scales larger than about 20 km (i.e., $10\Delta x$), as seen previously. However, at lower resolution, a second peak builds up at larger scale and becomes dominant at 10 and 20 km resolutions. This is in obvious disagreement with the $10\Delta x$ relation and the notion of effective resolution. At low resolution, dissipation affects the entire range of scale and reaches its maximum at large scale, which is generally unexpected.

To understand this behavior we can use the previous analysis of one-dimensional linear advection (Section 4.1). Spectral dissipation $D_H = \Im(\omega)E(k) \sim \nu_4 k^4 E(k)$. If kinetic energy $E(k)$ is considered constant, D_H evolves as k^4 (away from the grid scale) and Fig. 6 shows that it appears strong only for scales smaller than $10\Delta x$, consistent with the 2 km solution. However if $E(k)$ is variable in k , D_H depends explicitly on the energy spectrum slope. If it is steeper than -4 , i.e., the submesoscale range is not properly repre-

sented, dissipation tends to increase at large scale as in the coarse resolution ROMS solutions. To test our analysis, we reconstructed the dissipation term as $\nu_4 k^4 E(k)$ in Fig. 7 (dotted lines in bottom panel). The good match with the original term validates our scaling arguments based on the simplified advection equation.

Obviously, the concept of effective resolution is inappropriate in the low resolution cases as no part of the spectrum is safe from numerical dissipation. This is even worse if Laplacian instead of biharmonic diffusion is used since even a k^{-2} distribution for $E(k)$ does not prevent dissipation from increasing at large scale (as confirmed by experiments that are not shown here). On the contrary, this analysis argues in favor of hyperdiffusivity of higher order than fourth order, consistent with findings from Large Eddy Simulation studies (Frisch et al., 2008).

5. APE dissipation: spurious diapycnal mixing

Both vertical and horizontal advection schemes are subjected to spurious diapycnal mixing (Griffies et al., 2000; Marchesiello et al., 2009). Their effect, sometimes called Veronis effect, is to diffuse water masses and density slopes and lower the reservoir of potential energy available for ocean dynamics. In ROMS, spurious diapycnal mixing is essentially linked to lateral tracer advection. To circumvent this problem, a rotated isopycnal hyperdiffusion operator called RSUP3 (Marchesiello et al., 2009; Lemarié et al., 2012) was designed to take advantage of the split UP3 algorithm (Eq. (12)).

The impact of isopycnal diffusion is clearly visible on the KE spectrum (Fig. 8). The energy at large scale is similar to the standard solution (UP3 scheme), but at small scale the spectrum shows a considerable increase (a factor 3 is shown in the lower panel of Fig. 8). The dissipation range seems to recede and leave a well-defined submesoscale range of slope close to -2 , indicating an effective resolution more comparable to the 2 km solution (Fig. 7).

The KE increase can be associated with an increase in energy injection. Fig. 10 shows that submesoscale KE injection is extended to near the finest scale of the RSUP3 solution. The vertical profile of injection (Fig. 9) is close to that of the 2 km solution (Fig. 4), with large $w'b'$ subsurface signal. The reduction of spurious diapycnal mixing clearly boosts the source of submesoscale energy. Identically, the mean w_{RMS} vertical profile of the solution with isopycnal diffusion (left panel of Fig. 9) shows an increase in surface dynamics that can only be observed at the highest resolution of the reference simulations (Fig. 4). Limiting diapycnal diffusion results in sharper fronts and more intense surface currents.

It is generally assumed that eddy-resolving models would not require a particular treatment of the Veronis effect since lateral numerical diffusion (whether explicit or implicit) would be small enough. This argument has been opposed by Roberts and Marshall (1998), who show that spurious diapycnal mixing scales with both the lateral diffusion coefficient and vorticity gradients. Since vorticity gradients cascade to smaller scales, a decrease of the diffusion coefficient with increased resolution does not guaranty a decrease of spurious diapycnal mixing in the mesoscale and submesoscale ranges. In addition to this dynamical argument by Roberts and Marshall (1998), we note that the numerical diapycnal diffusivity A_D does not decrease rapidly with resolution. A_D scales as $A_H^{UP3} S^2$ (Redi, 1982), with S the isopycnal slope of order 0.01, and $A_H^{UP3} \approx \nu_4/L^2 \approx \frac{1}{12} U \Delta x^3/L^2$ (U is a velocity scale of order 0.1 m/s and L a mixing length scale of order $10\Delta x$). We find that A_D becomes small (compared with diapycnal mixing from microscale processes: $K_\rho \sim 10^{-5} \text{m}^2/\text{s}$) only when the grid resolution is finer than 100 m. Therefore, advection schemes using either implicit diffusion for damping dispersive errors or flux correction for preserving monotonicity must be handled with care, even in the eddy-resolving regime. Their effect is to suppress submesoscale KE

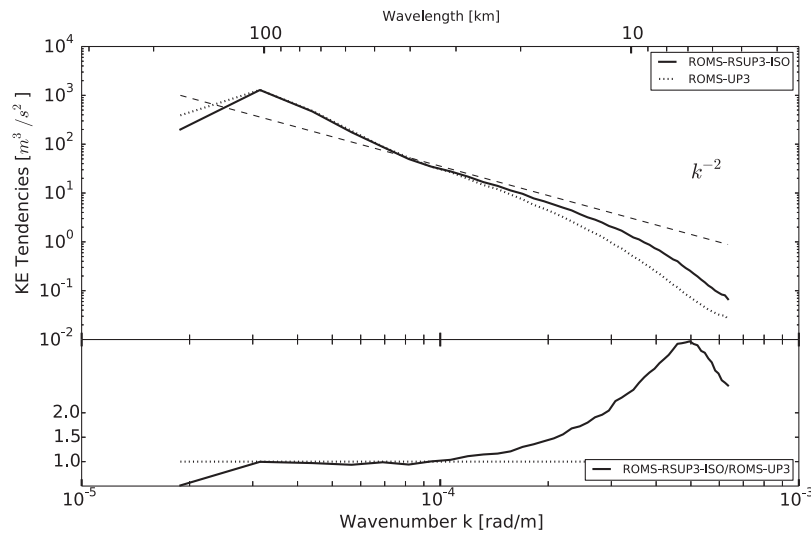


Fig. 8. Sensitivity of surface KE spectra to spurious diapycnal mixing in ROMS at 5 km resolution. Top panel: solutions with rotated isopycnal hyperdiffusion operator RSUP3 (plain line), standard UP3 advection scheme (dotted line). Bottom panel: ratio of the two spectra in linear scale (RSUP3/UP3) showing a ratio much greater than unity over the submesoscale and dissipation ranges.

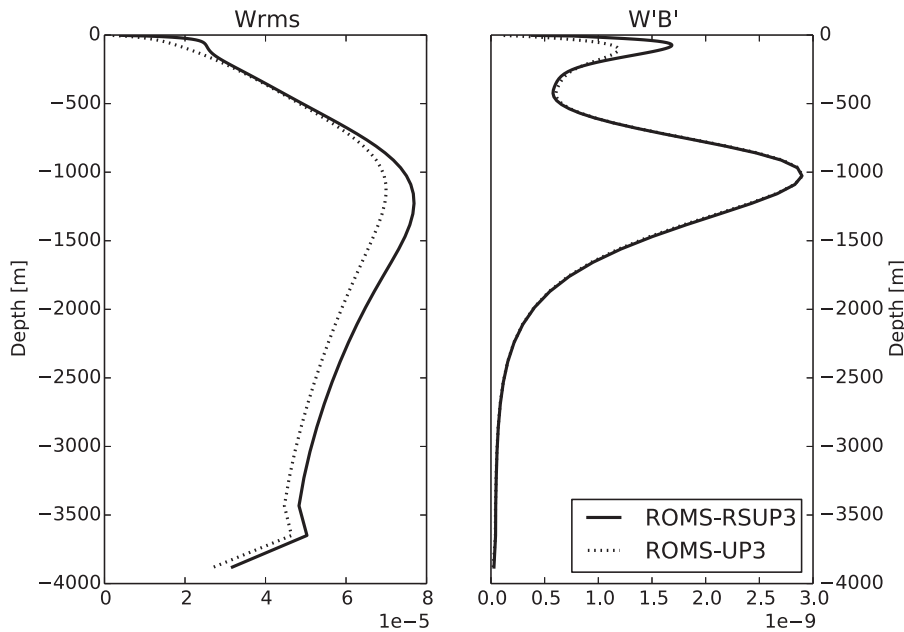


Fig. 9. 20-year mean vertical profiles of RMS vertical velocity $\sqrt{w'^2}$ (m^2/s^2) and eddy buoyancy flux $\overline{w'b'}$ (m^2/s^3) at 5 km resolution: solutions with rotated isopycnal hyperdiffusion operator RSUP3 (plain line) and standard UP3 advection scheme (dotted line).

injection as the supply of APE needed to sustain frontal processes can be rapidly drained by diapycnal diffusion.

6. KE dissipation: temporal filters

When better accuracy is desired for a model, developers generally address the problem of spatial discretization. Temporal discretization is harder to improve as it imposes thorough restructuring of the model kernel. The question is: how important is temporal discretization to model accuracy and how do temporal filters work? A comparison of models is a difficult task as so many parameters can potentially impact on the solution. Nevertheless, the intercomparison is useful to give a realistic measure of the model sensitivity to numerical choices. For this exercise, the configurations of ROMS and NEMO are taken as close as possible. The same horizontal and vertical grids and same spatial discretization

for momentum and tracer advection are used. The largest differences come from the temporal filters.

6.1. Model intercomparison

Fig. 3 presents a comparison of surface vorticity in ROMS and NEMO for different resolutions. The color bar is fixed for all plots so the difference of color intensity does reflect a difference of vorticity amplitude. The two models have a generally comparable behavior and resolution sensitivity. They have similar mesoscale activity with vorticity fronts sharpening at finer resolution. However, ROMS shows slightly sharper vorticity fronts at each resolution. At 2 km resolution, numerous submesoscale eddies are apparent in ROMS that are fewer in NEMO. This is particularly true in the northern part of the domain where the deformation radius is lower (~ 25 km at the northern boundary compared with ~ 35 km at the

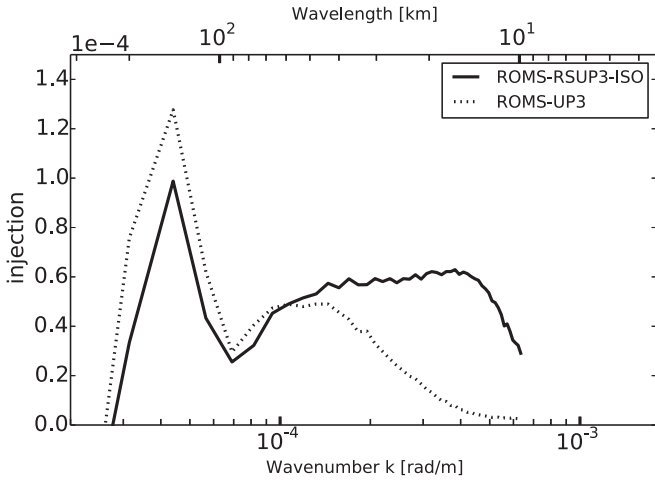


Fig. 10. Sensitivity of surface injection spectra to spurious diapycnal mixing in ROMS at 5 km resolution. Solutions with rotated isopycnal hyperdiffusion RSUP3 (plain line) and standard UP3 advection scheme (dotted line).

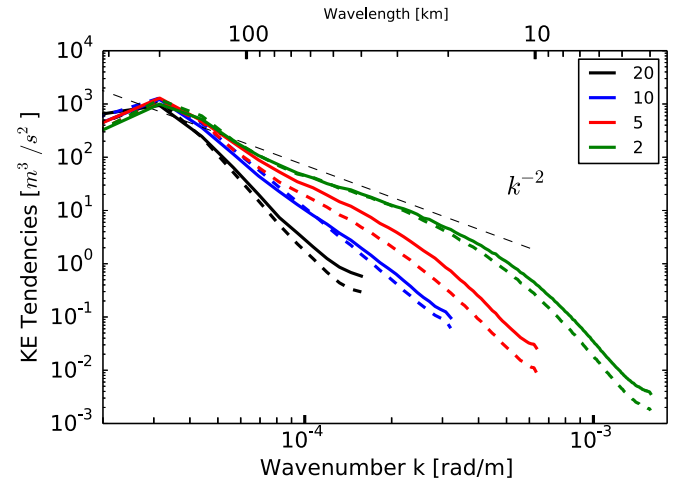


Fig. 12. Near surface KE spectra (m^3/s^2) for ROMS (solid lines) and NEMO (dashed lines) at 20 km, 10 km, 5 km and 2 km resolution.

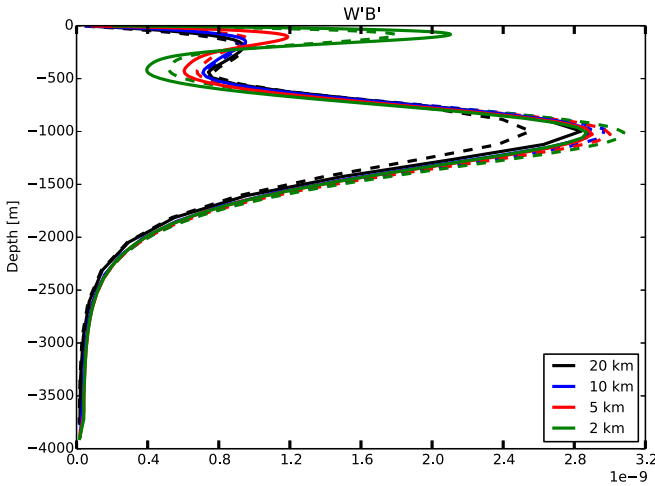


Fig. 11. 20-year mean vertical profiles of eddy buoyancy flux $\overline{w'b'}$ (m^2/s^3) for ROMS (solid lines) and NEMO (dashed lines) at 20 km, 10 km, 5 km and 2 km resolution.

southern boundary), requiring a higher accuracy there for frontal processes to develop.

Fig. 11 shows together the dynamical profiles of ROMS and NEMO. Confidence intervals were computed (not shown) and the differences observed here are significant. The most important difference is observed in the conversion of energy near the surface at 5 km resolution. At this resolution, ROMS starts showing large amount of surface KE injection associated with submesoscale activity. NEMO, on the other hand, needs higher resolution and only gets a substantial increase of KE injection at 2 km resolution.

The kinetic energy spectrum is consistent with this analysis showing that the dissipation range in NEMO starts at lower k (Fig. 12). In the submesoscale range, at high resolution, ROMS and NEMO show a ~ -2 power law, which drops when entering the dissipation range (around the 20 km scale $\sim 10\Delta x$ for ROMS and slightly larger scale for NEMO).

6.2. The Robert-Asselin filter

Several tests were performed to investigate the cause of differences in energy spectra between the two models. Because long integration time is necessary for differences to be statistically reliable, we concentrate on the 5 km resolution solutions, which

marginally represent submesoscale dynamics and thus present the largest differences between models. A noticeable difference between the two numerical models of interest is the time-stepping algorithm. Like the vast majority of oceanic climate models, NEMO is discretized using a leapfrog scheme while ROMS uses the third-order predictor-corrector LF-AM3 scheme. The reader is referred to Lemarié et al. (2015) for a detailed comparison between of the two methods in terms of stability, accuracy and robustness (summarized in Section 2). Robustness is defined here as the preservation of scheme performances as the Courant number $\alpha_{\text{adv}} = u\Delta t/\Delta x$ varies across its range of stability. A weakness of both LF and LF-AM3 is the presence of a $2\Delta t$ computational mode (it only appears in LF-AM3 when combined with the advection scheme, not in the semi-discrete form; Lemarié et al., 2015). However, this mode in LF-AM3 is not generally harmful because it is efficiently damped by the implicit high-order dissipation of the scheme. The problem is more acute for LF that leaves the computational mode undamped, even for well-resolved scales. As a consequence, a low-order temporal filter must be added. Historically, the preferred choice is the Robert–Asselin (RA) filter.

The RA filter has several known drawbacks (e.g., Durran, 1991; 2010): reduction of the stability range, additional dispersive errors⁷ and damping of the physical mode. In order to assess the extra-dissipation associated with this family of filters let us consider again the one-dimensional advection equation semi-discretized in time using a leapfrog scheme combined with a temporal filter⁸ with coefficient γ :

$$\frac{u^{n+1} - u^{n-1}}{2\Delta t} + \left[\frac{\gamma \Delta t}{2} \right] \left(\frac{u^n - 2u^{n-1} + u^{n-2}}{\Delta t^2} \right) + c_0 \frac{\partial u^n}{\partial t} = 0. \quad (18)$$

A common value for the dimensionless filter coefficient γ in realistic applications is $\gamma \approx 0.1$. The truncation error \mathcal{E} associated with time discretization of Eq. (18) is:

$$\mathcal{E} = \frac{\gamma \Delta t}{2} \frac{\partial^2 u}{\partial t^2} + \frac{(1 + 3\gamma)\Delta t^2}{6} \frac{\partial^3 u}{\partial t^3} + \mathcal{O}(\Delta t^3),$$

⁷ The RA filter is known to accelerate high wavenumbers in addition to already present acceleration due to unfiltered Leapfrog itself (Durran, 1991). This may be partially compensated by the combination of second-order centered spatial schemes at maximum stable Courant number. However, the cancellation of dispersive errors is lost when Leapfrog is used in combination with a high-order spatial scheme. In any case, realistic applications of ocean modeling have a large range of Courant numbers that undermines the practical utility of LF-RA.

⁸ A Laplacian rather than traditional Robert–Asselin filter is used here for simplicity. The two have similar dissipative properties (Marsaleix et al., 2012), and our conclusions are not affected by this choice.

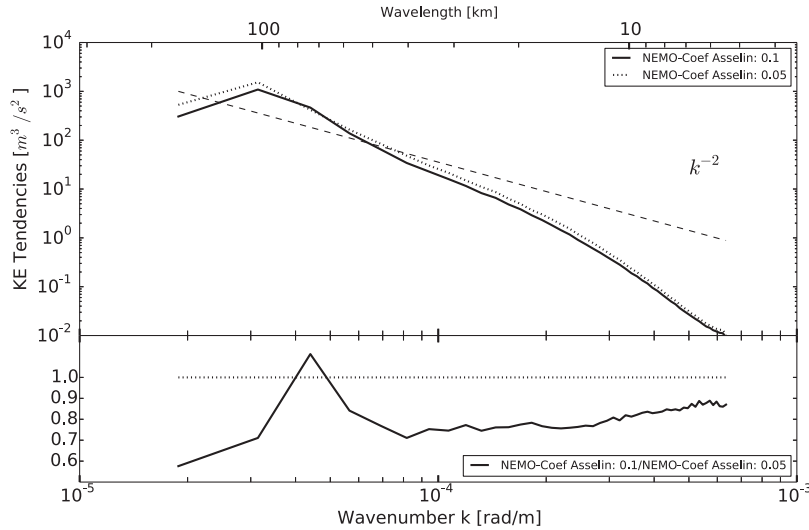


Fig. 13. Sensitivity of surface KE spectrum to the Asselin coefficient at 5 km resolution in NEMO. Top panel: solutions for the standard coefficient value of 0.1 (plain line) and the reduced value of 0.05 (dotted line). Bottom panel: ratio of the two spectra in linear scale showing higher energy levels over a wide range of scales when a reduced filter coefficient is used (ratio < 1).

showing that the filtered LF is degraded to first-order accuracy. Using again the linear advection equation, we can express the temporal derivatives in terms of spatial derivatives:

$$\varepsilon = \frac{c_0^2 \gamma \Delta t}{2} \frac{\partial^2 u}{\partial x^2} + \mathcal{O}(\Delta t^2) = \gamma \alpha_{\text{adv}} A_H^{\text{UP1}} \frac{\partial^2 u}{\partial x^2} + \mathcal{O}(\Delta t^2). \quad (19)$$

$A_H^{\text{UP1}} = c_0 \Delta x / 2$ is the implicit diffusivity of a first-order upwind scheme, i.e., a measure of strong numerical damping. The time filter is thus equivalent to a spatial Laplacian diffusion with coefficient $\gamma \alpha_{\text{adv}} A_H^{\text{UP1}}$ where the filter's damping effect is modulated by the $\gamma \alpha_{\text{adv}}$ product. This analysis is strictly valid for the advection equation, not for the full set of equations solved by a numerical model, but we expect general conclusions to hold.

We conducted some tests on the Asselin coefficient with NEMO on the Baroclinic jet test case. In Fig. 13, an Asselin coefficient of 0.05 instead of 0.1 (standard value) gives a KE spectrum with slightly higher energy at all k (recall from the previous section that a Laplacian diffusion operator affects the whole spectrum). If this result was expected, the impact is however moderate. The reason is that in the Baroclinic jet test case the stability limit is given by internal gravity waves, not advection, because there is no surface forcing. The advection Courant number remains quite small at ~ 0.1 , which yields an equivalent horizontal diffusivity of $10^{-2} A_H^{\text{UP1}}$, i.e., around $10 \text{ m}^2/\text{s}$ at 5 km resolution.

A partner study by Jouanno et al. (2015) shows results consistent with our interpretation. In their configuration of a baroclinic jet forced with high-frequency winds of extra-tropical storms, intense inertial waves are excited with Courant numbers closer to 1. In their case, the Asselin filter has a significant effect and is responsible for 20% of KE dissipation when Δt is near the stability limit. These results also underline the drawback of methods for increasing the permissible time stepping associated with internal gravity waves — this is commonly done in global applications through time-averaging of the pressure gradient as in Brown and Campana (1978) — as they lead to increasing the advection Courant number. An important property of a time stepping scheme is thus its robustness with respect to the Courant number (Lemarié et al., 2015). The Leapfrog scheme is a counter-example of that.

In addition to its effect on KE dissipation, the time filter also affects KE injection through diapycnal diffusion. The linear analysis above is also valid for tracers. A small amount of lateral density diffusion can translate into large amounts of diapycnal diffusion

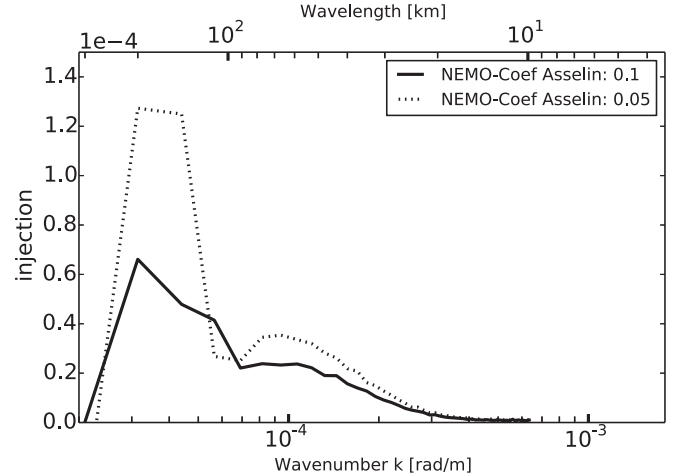


Fig. 14. Sensitivity of surface injection spectra to the Asselin filter coefficient in NEMO at 5 km resolution. In plain line the standard value of 0.1 is used. In dotted line this value is reduced to 0.05.

near density slopes (Section 5). Fig. 14 shows that the run with a reduced filter coefficient gets substantially stronger KE injection at small scale. It suggests lesser diapycnal diffusion, preserving APE and its conversion to KE, as for the isopycnal diffusion operator in Section 5.

6.3. The 2D/3D coupling filter

Another notable difference in the models comes from the treatment of the fast barotropic mode. Most ocean models use a split-explicit, free-surface paradigm, where short time steps are used to advance the surface elevation and barotropic momentum, and a larger time step is used for temperature, salinity, and baroclinic momentum. Barotropic variables are advanced with a vertical integration of 3D momentum equations; the result is filtered across the baroclinic time step to avoid aliasing and is then fed back to the 3D momentum calculation. This is the barotropic/baroclinic or 2D/3D coupling (Shchepetkin and McWilliams, 2005). Splitting errors can be introduced in the coupling process that can affect model stability. A known cause for splitting errors is the spurious vertical shear introduced with Boussinesq approximation

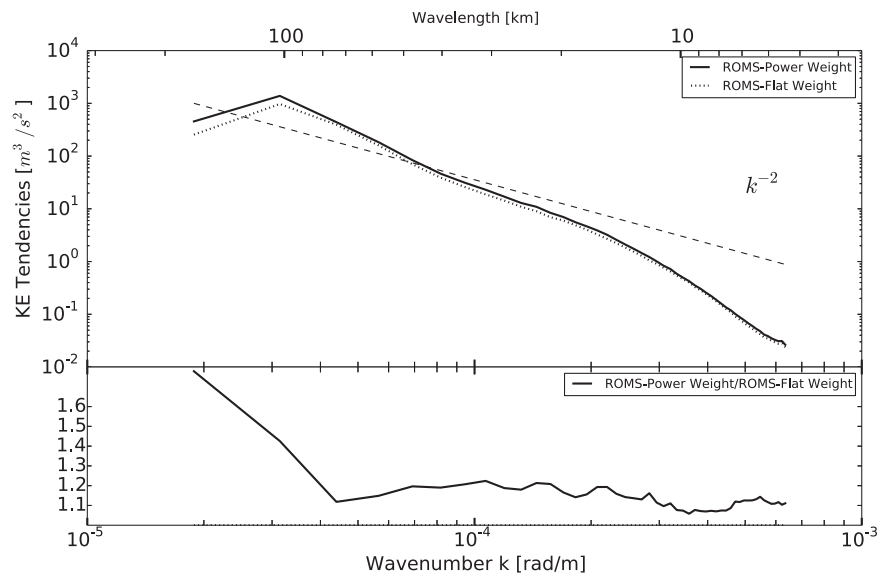


Fig. 15. Sensitivity of surface KE spectra to the 2D/3D coupling filter in ROMS at 5 km resolution. Top panel: solutions with standard power-law filter (plain line) and flat-weight averaging (dotted line). Bottom panel: ratio of the two spectra in linear scale.

when computing the pressure gradient acceleration (Higdon and de Szoeke, 1997; Shchepetkin and McWilliams, 2011). In ROMS, a pressure gradient correction in the barotropic mode can efficiently remove this error and allow less dissipative filtering of the barotropic mode: currently, a second-order accurate power-law filter (Shchepetkin and McWilliams, 2005) rather than the more traditional first-order flat-weight averaging operator (used in NEMO as in many other ocean general circulation models). Another source of splitting error is due to the fact that the true barotropic mode (given by an eigenmode decomposition) is depth-dependent. Because its vertical variations are small, approximation of the barotropic mode as the depth-integrated flow is justified (Dukowicz, 2006). However, it is a source of numerical instability if undamped⁹ (Demange et al., 2014). Whether for aliasing or splitting issues, some form of filter of the barotropic mode is needed but its effect on realistic physical solutions is unknown (in ideal cases, see the analysis of barotropic waves response to time differencing in Dukowicz and Smith, 1994).

To contribute on the subject, we tested the flat-weight against power-law averaging procedure in ROMS. Fig. 15 shows a significant increase of dissipation with the flat filter (the log scale may be misleading as it tends to conceal some of the differences but observe the ratio of energy spectra in the lower panel). Interestingly, this effect appears over a large range of scales but the smallest. The barotropic mode is strong at mesoscale and large scale while small scales are more surface trapped and weakly contribute to the depth-average energy. Therefore, barotropic mode filters do not affect effective resolution as a scale-selective dissipation mechanism (as assumed in Skamarock, 2004), but have a more diffuse impact across the spectrum that can only be reduced through better control of splitting errors (Shchepetkin and McWilliams, 2005; Demange et al., 2014).

Note that implicit time-stepping of the 2D mode is an alternative to the time splitting approach. It avoids aliasing and splitting errors as baroclinic and barotropic modes are advanced with the same time step. However, they have drawbacks in terms of accuracy (large dispersive or diffusive errors with large time steps; Dukowicz and Smith, 1994) and performance on parallel computers, especially at high resolution (problem- and machine-

dependent solver optimization is then needed to overcome poor scalability). Most current ocean models use a time splitting approach.

7. Conclusion

The increase of model resolution naturally leads to the representation of a wider energy spectrum. As a result, in recent years, the understanding of oceanic submesoscale dynamics has significantly improved. However, dissipation in submesoscale models remains dominated by numerical constraints rather than physical ones. Effective resolution has been defined by the numerical dissipation range, which is a function of a model's numerical filters. We present a baroclinic jet test case, which provides a controllable test of a model capacity at resolving submesoscale dynamics. We compare analyses performed on simulations from two models, ROMS and NEMO, at different mesh sizes (from 20 to 2 km). Through a spectral decomposition of kinetic energy and its budget terms, we identify the characteristics of numerical dissipation and effective resolution.

We show that numerical dissipation appears in different parts of a model, especially in spatial advection-diffusion schemes for momentum equations (KE dissipation) and tracer equations (APE dissipation) and in the time stepping algorithms. Dissipation does not always decay at large scale and we conclude that the definition of effective resolution is not always meaningful, depending on mesh size and numerical methods. Our results argue in favor of high-order filters (higher than fourth order) for the dissipation range to be always restricted to small scales. For example, a sixth-order spectral dissipation $D(k) = \nu_6 k^6 E(k)$ would remain a decreasing function of wavelength even for steep energy slopes and thus insure a more restricted dissipation range. To avoid dispersive errors, advection schemes must be consistent with the dissipation operator and be of higher order as well. We show from a linear analysis that upwind schemes present an optimal combination of advection/diffusion because, for any odd-order of accuracy, their damping factor is always proportional to dispersive errors (at any wavenumber).

Changes in spatial schemes must also be consistent with the temporal scheme. The combination of low-order temporal schemes and high-order spatial schemes generally show poor performances for dispersion/diffusion properties and for robustness with

⁹ Topography complicates further the internal-external mode decomposition but this is not relevant for the present study

respect to the Courant number (Durran, 1991; Shchepetkin and McWilliams, 1998; 2009; Lemarié et al., 2015). The latter property is particularly relevant to ocean modeling. Any scheme can always be made to work its best in a particular range of resolution, but realistic applications have a large range of Courant number. We show that a Laplacian time filter (equivalently, the Asselin filter), often used with the Leapfrog scheme, is equivalent to a spatial Laplacian filter with coefficient depending on the advection Courant number. If the Courant number is far from its maximum value allowed for stability, then the equivalent diffusion coefficient is small. In this sense, the Baroclinic jet test case is permissive.

Besides the internal mode filter, we show that another source of dissipation is the barotropic mode time filter that is required for mode coupling in split-explicit ocean models. Contrarily to other spatial and temporal filters in the model, this one is not even scale-selective by construction as it affects barotropic waves with large spatial scales. Therefore, it does not fit in the common concept of effective resolution (Skamarock, 2004). Yet, higher-order filters or diffusive barotropic time stepping schemes can be used that reduce their impact on the KE spectrum but only at the condition of a better control of splitting errors. Demange et al. (2014) show that there is room for improvement there.

It is generally assumed that eddy-resolving models have only small spurious diapycnal mixing (Veronis effect) associated with numerical necessities. This argument has been opposed by Roberts and Marshall (1998) on the basis of dynamic arguments linking spurious mixing and direct cascading of vorticity gradients. Our results agree with that, showing kinetic energy spectrum to be very sensitive to mixing orientation at submesoscale. The effect of spurious diapycnal mixing is to suppress submesoscale KE injection by draining the supply of APE, which is needed to sustain frontal processes. It argues in favor of third-order rotated diffusion schemes such as RSUP3 (Marchesiello et al., 2009) or much higher-order advection/diffusion methods. In some additional experiments (not shown), the use of fifth-order upwind or fifth-order Weighted Essentially Non-Oscillatory scheme (Jiang and Shu, 1996) did not reduce diapycnal mixing as much as RSUP3. Other tests pointed to vertical density advection as a potential source of diapycnal mixing. Specifically, NEMO's flux correction to second-order centered advection (C2-FCT) produced some spurious mixing, albeit to a more limited extent than geopotential diffusion. This error explained part of the differences between ROMS and NEMO besides temporal filters. Nonlinear (non-oscillatory) advection schemes are thus not immune to diapycnal mixing errors.

Finally, efficiency of numerical methods should be assessed with respect to their computational cost. A generic estimation by Sanderson (1998) suggests that low-order differencing is a costly choice to achieve a given accuracy and that differencing order must roughly equal model dimension (4 here) to ensure that grid refinement reduces truncation error faster than computational cost increases. There are several critical assumptions in this estimation. In our experiments (Section 2.3), the predictor-corrector time integration scheme in ROMS is systematically faster than the Leapfrog scheme in NEMO, despite extra-cost of a two-stage time stepping. This result can be largely explained by the extended range of stability for both the fast and slow modes. Therefore, adding complexity to the temporal schemes can be beneficial rather than detrimental to computational costs, making high-order methods at even higher advantage than assumed from simple scaling arguments. The upgrade of time stepping algorithms in ocean models, central piece of the computational kernel, can be a cumbersome task but appears critical from our results, not just as a matter of model solution quality but also of computational efficiency.

To conclude, our results indicate that effective resolution, defined by scale-selective dissipation, is inadequate to qualify general circulation ocean models with low-order spatial and temporal

filters, even at high grid resolution. High-order methods are better suited to the concept and probably unavoidable. Fourth-order filters are suited only for grid resolutions less than a few kilometers and momentum advection schemes of even higher-order should provide more robustness in confining the dissipation range. Effective resolution is also shaken by the need for non scale-selective barotropic mode filters. But, the most surprising effect came from APE dissipation through spurious diapycnal mixing at submesoscale, which poses again the longstanding question of precisely how much vertical diffusion is at work in the real ocean.

Acknowledgments

This research has received support from grants by ANR (CO-MODO: ANR-11-MONU-005 and SMOC). This work was performed using HPC resources from CALMIP (Grant 2014-P1402) and from CURIE (PRACE Project ra1616). The authors thank three anonymous reviewers for their detailed and insightful comments on the manuscript.

Appendix A. Initialization of the Baroclinic jet test case

The initial density field is constructed with dense and light density profiles in the northern and southern regions, $\rho_N(z)$ and $\rho_S(z)$, which are defined as follows:

- a distorted hyperbolic tangent density profile to produce the interior meridional density gradient (and interior baroclinic instability) but with no contribution to the surface meridional density gradient;
- a hyperbolic tangent density profile for the southern region only, which has its inflection point close to the surface; this is responsible for surface meridional density gradients generating the Charney instability;
- a small depth-independent background stratification that applies equally to the northern and southern profiles and guarantees static stability.

Precisely, we have:

$$\rho_{N,S}(z) = \rho^{max} - S_b(z+h) - \frac{1}{2} \delta \rho_{N,S}^{int} \left[1 + \tanh\left(\frac{d_{N,S}(z) - z_{N,S}^{int}}{\delta z_{N,S}}\right) \right] - \frac{1}{2 \tanh(1)} \delta \rho_{N,S}^{surf} \left[1 + \tanh\left(\frac{z^{surf} - z}{z^{surf}}\right) \right] \quad (A.1)$$

where:

$$d_{N,S}(z) = z_{N,S}^{int} + (z - z_{N,S}^{int}) \left[1 + 0.5 \left(\frac{z - z_{N,S}^{int} + |z - z_{N,S}^{int}|}{1.3 \delta z_{N,S}} \right)^2 \right]^{0.5} \quad (A.2)$$

$$\delta \rho_N^{int} = \delta \rho_S^{int} \left[1 + \tanh\left(\frac{d_S(0) - z_S^{int}}{\delta z_S}\right) \right] / \left[1 + \tanh\left(\frac{d_N(0) - z_N^{int}}{\delta z_N}\right) \right] \quad (A.3)$$

z denotes depth, h is the ocean depth (4000 m), $\rho_{max} = 27.75 \text{ kg m}^{-3}$, $S_b = 9.8 \cdot 10^{-6} \text{ kg m}^{-4}$, $\delta \rho_{N,S}^{int} = 1.41/1.4$ (guarantees that the first hyperbolic tangent term in (A.1) does not contribute to the surface meridional density difference), $z_{N,S}^{int} = -400/-1000$, $\delta z_{N,S} = 300/700$, $\delta \rho_{N,S}^{surf} = 0/1.5$, $z^{surf} = -300$.

The water within 200 km from the northern (resp. southern) boundary is homogeneous and has its density equal to the dense (resp., light) profile. In the center of the channel, density goes smoothly from light to dense over a length scale $L_{jet} = 1600 \text{ km}$

and the frontal zone is concentrated in a ~ 1000 km wide central region. The connection involves a function F_{yz} defined as:

$$\begin{aligned} F_{yz}(y) &= 1 & \text{if } y < 0 \\ F_{yz}(y) &= 0 & \text{if } y > \pi \\ F_{yz}(y) &= 1.0 - (y - \sin(y) * \cos(y))/\pi & \text{otherwise} \end{aligned} \quad (\text{A.4})$$

F_{yz} resembles a tanh function but it is exactly constant when approaching the northern and southern walls. y is a transformed coordinate for the meridional direction:

$$y = \pi \cdot \frac{L_y}{L_{jet}} [-0.5 : 1/N_y : 0.5] + \pi/2 \quad (\text{A.5})$$

The jet destabilization is triggered by a very small random density perturbation. The perturbation is introduced by adding an x and z dependency to the connection between northern and southern profile through modification of the y coordinate: $y \rightarrow y(x, z)$. Initial zonal velocities are in geostrophic balance with the resulting density field with the level of no motion set at the bottom.

Appendix B. Analysis of arbitrary-order upwind advection schemes

The purpose of this section is to analyze the dissipatively dominant truncation error of odd-ordered advection schemes. We consider the one-dimensional advection equation for a cell-centered quantity q with constant positive velocity $c_0 > 0$. Let us first introduce a generic linear discretization of successive derivatives based on a centered formula for even-ordered derivatives and upwind formula for odd-ordered derivatives (assuming $c_0 > 0$):

$$\begin{cases} \mathbf{D}_1 = (q_i - q_{i-1})/\Delta x \\ \mathbf{D}_2 = (q_{i+1} - 2q_i + q_{i-1})/\Delta x \\ \mathbf{D}_3 = (q_{i+1} - 3q_i + 3q_{i-1} - q_{i-2})/\Delta x \\ \vdots \\ \mathbf{D}_p = \left(\sum_{n=0}^p (-1)^n C_p^n q_{i+m-n} \right) / \Delta x, \\ m = \lfloor p/2 \rfloor = \max \{q \in \mathbb{Z}; q \leq p/2\} \end{cases} \quad (\text{B.1})$$

where C_p^n is the usual binomial coefficient $C_p^n = \frac{p!}{n!(p-n)!}$. It is straightforward to show that an order p linear advection scheme can be written as a linear combination of \mathbf{D}_n terms:

$$c_0 \frac{\tilde{q}_{i+\frac{1}{2}}^p - \tilde{q}_{i-\frac{1}{2}}^p}{\Delta x} = c_0 \sum_{n=1}^p \gamma_n \mathbf{D}_n, \quad (\text{B.2})$$

where $\tilde{q}_{i+\frac{1}{2}}^p$ is the order p interfacial approximation of q . The coefficients γ_n are chosen based on a Taylor series expansion to reach the expected order of accuracy. A general formula to obtain the coefficients γ_n is:

$$\gamma_1 = 1, \quad \gamma_n = \prod_{l=2}^n (-1)^l \frac{\lfloor l/2 \rfloor!}{l!} \quad \text{for } n \geq 2, \quad (\text{B.3})$$

where the notation $\lfloor l/2 \rfloor$ is defined in (B.1). Using equations (B.1, B.2, B.3), linear advection schemes of any order p can be derived. For example, we recover the first-order upwind scheme for $\gamma_1 = 1$ and $\gamma_n = 0$ for $n \geq 2$; the third-order upwind scheme for $\gamma_1 = 1$, $\gamma_2 = 1/2$, $\gamma_3 = -1/6$ and $\gamma_n = 0$ for $n \geq 4$, and so on. these formula are valid only for $c_0 > 0$; in the case $c_0 < 0$, upwinding for odd-ordered derivatives in (B.1) must be done in the opposite direction.

After some simple algebra, the Fourier transform of \mathbf{D}_n terms can be obtained in a generic way:

$$\gamma_n \widehat{\mathbf{D}}_n = \begin{cases} \gamma_n \{2(\cos(k\Delta x) - 1)\}^{n/2} / \Delta x, & \text{for even } n \\ \gamma_n (i \sin(k\Delta x) \{2(\cos(k\Delta x) - 1)\}^{(n-1)/2} / \Delta x - \widehat{\mathbf{D}}_{n+1}/2), & \text{for odd } n \end{cases} \quad (\text{B.4})$$

with k the wavenumber. Given that $\gamma_{n+1} = \gamma_n/2$ for odd n , we can rewrite the formula for $\gamma_n \widehat{\mathbf{D}}_n$ as:

$$\gamma_n \widehat{\mathbf{D}}_n = \begin{cases} \gamma_n \{2(\cos(k\Delta x) - 1)\}^{n/2} / \Delta x, & \text{for even } n \\ i \gamma_n \sin(k\Delta x) \{2(\cos(k\Delta x) - 1)\}^{(n-1)/2} / \Delta x - \gamma_{n+1} \widehat{\mathbf{D}}_{n+1}, & \text{for odd } n \end{cases} \quad (\text{B.5})$$

From (B.5) and (B.2) we deduce the general form of the dispersion relation associated with a linear advection scheme of order p :

$$\omega(k) = -i \left[c_0 \sum_{n=1}^p \gamma_n \widehat{\mathbf{D}}_n \right]$$

First, we note that the imaginary part of ω is straightforward from (B.5) since $\Im(-i\gamma_n \widehat{\mathbf{D}}_n) = -\gamma_n \widehat{\mathbf{D}}_n$ for even values of n and $\Im(-i\gamma_n \widehat{\mathbf{D}}_n) = \gamma_{n+1} \widehat{\mathbf{D}}_{n+1}$ for odd values of n . By successive elimination of the $\gamma_n \widehat{\mathbf{D}}_n$ terms in the summation between odd and even values of n , we simply get:

$$\Im(\omega) = c_0 \sum_{n=1}^p \Im(i\gamma_n \widehat{\mathbf{D}}_n) = \begin{cases} c_0 \gamma_{p+1} \widehat{\mathbf{D}}_{p+1}, & \text{for odd } p \\ 0, & \text{for even } p \end{cases} \quad (\text{B.6})$$

This result states that even-ordered advection schemes are purely advective schemes while odd-ordered advection schemes have a nonzero dissipative component. From (B.6), we also remark that the leading order term in the truncation error of an order p upwind scheme is a diffusive operator of order $p+1$ with coefficient $c_0 \gamma_p \Delta x^p$. Since $\gamma_2 = 1/2$ and $\gamma_4 = -1/12$ we recover the well-known results that dissipation associated with first- and third-order upwind schemes is respectively a Laplacian operator with coefficient $c_0 \Delta x/2$ and a biharmonic operator with coefficient $c_0 \Delta x^3/12$.

Now looking at the group velocity, the exact value for the advection equation is c_0 while the numerical group velocity c_g^p for an order p scheme is given by:

$$c_g^p = \frac{d\Re(\omega)}{dk} = c_0 \sum_{n=1}^p \frac{d\Re(-i\gamma_n \widehat{\mathbf{D}}_n)}{dk}.$$

Because $\Re(-i\gamma_n \widehat{\mathbf{D}}_n) = 0$ for even values of n , only odd indices contribute to c_g^p . After some algebra we find:

$$\begin{aligned} \frac{d\Re(-i\gamma_n \widehat{\mathbf{D}}_n)}{dk} &= \frac{d}{dk} (\gamma_n \sin(k\Delta x) \{2(\cos(k\Delta x) - 1)\}^{(n-1)/2} / \Delta x) \\ &= \gamma_n (\cos k\Delta x \{2(\cos(k\Delta x) - 1)\}^{(n-1)/2} \\ &\quad - (n-1) \sin^2 k\Delta x \{2(\cos(k\Delta x) - 1)\}^{(n-3)/2}) \\ &= n \gamma_n \{2(\cos(k\Delta x) - 1)\}^{(n-1)/2} \\ &\quad + \gamma_n \frac{n+1}{4} \{2(\cos(k\Delta x) - 1)\}^{(n+1)/2} \end{aligned} \quad (\text{B.7})$$

Given that $\gamma_{n+1} = \gamma_n/2$ for odd indices, the second term in (B.7) is equivalent to:

$$\gamma_n \frac{n+1}{4} \{2(\cos(k\Delta x) - 1)\}^{(n+1)/2} = \frac{n+1}{2} \gamma_{n+1} \widehat{\mathbf{D}}_{n+1} \Delta x.$$

The first term in (B.7) equals 1 for $n = 1$, and can be generalized for $n > 1$ as:

$$n \gamma_n \{2(\cos(k\Delta x) - 1)\}^{(n-1)/2} = -\frac{n-1}{2} \gamma_{n-1} \widehat{\mathbf{D}}_{n-1} \Delta x$$

since $\gamma_n = -\frac{n-1}{2n}\gamma_{n-1}$ for odd indices. As a result, (B.7) becomes:

$$\frac{d\mathfrak{N}(-i\gamma_n\widehat{\mathbf{D}}_n)}{dk} = \begin{cases} 1 + \gamma_2\widehat{\mathbf{D}}_2\Delta x, & \text{for } n = 1 \\ -\frac{n-1}{2}\gamma_{n-1}\widehat{\mathbf{D}}_{n-1}\Delta x \\ + \frac{n+1}{2}\gamma_{n+1}\widehat{\mathbf{D}}_{n+1}\Delta x, & \text{for odd } n > 1 \end{cases} \quad (\text{B.8})$$

Due to the successive cancellation of the $\frac{n+1}{2}\gamma_{n+1}\widehat{\mathbf{D}}_{n+1}\Delta x$ terms after summation, we get:

$$c_g^p = c_0 \sum_{n=1}^p \frac{d\mathfrak{N}(-i\gamma_n\widehat{\mathbf{D}}_n)}{dk} = c_0 \left[1 + \frac{p+1}{2}\gamma_{p+1}\widehat{\mathbf{D}}_{p+1}\Delta x \right] \quad (\text{B.9})$$

Combining (B.6) and (B.9), which holds for any arbitrary-order upwind linear advection scheme, we can derive a general relationship between the implicit dissipation of an upwind advection scheme of order p and dispersion associated with its group velocity error ($c_0 - c_g^p$):

$$\mathfrak{S}(\omega) = -2 \left[\frac{c_0 - c_g^p}{(p+1)\Delta x} \right]. \quad (\text{B.10})$$

References

- Blumen, W., 1978. Uniform potential vorticity flow: Part i. theory of wave interactions and two-dimensional turbulence. *J. Atmos. Sci.* 35 (5), 774–783. doi:10.1175/1520-0469(1978)035<0774:upvfpfi>2.0.co;2.
- Boyd, J.P., 1992. The energy spectrum of fronts: Time evolution of shocks in Burgers equation. *J. Atmos. Sci.* 49 (2), 128–139.
- Brown, J.A., Campana, K.A., 1978. An economical time-differencing system for numerical weather prediction. *Mon. Weather Rev.* 106, 1125–1136.
- Callies, J., Ferrari, R., 2013. Interpreting energy and tracer spectra of upper-ocean turbulence in the submesoscale range (1–200 km). *J. Phys. Oceanogr.* 43 (11), 2456–2474. doi:10.1175/jpo-d-13-063.1.
- Capet, X., G., R., A., P., Klein, P., G., M., 2014. Intensification of upper ocean quasi-balanced turbulence through charney instability. *J. Phys. Oceanogr.* Submitted.
- Capet, X., Klein, P., Hua, B.L., Lapeyre, G., McWilliams, J.C., 2008a. Surface kinetic energy transfer in surface quasi-geostrophic flows. *J. Fluid Mech.* 604, 165–174. doi:10.1017/S0022112008001110.
- Capet, X., McWilliams, J.C., Molemaker, M.J., Shchepetkin, A.F., 2008b. Mesoscale to submesoscale transition in the California current system. part i: Flow structure, eddy flux, and observational tests. *J. Phys. Oceanogr.* 38 (1), 29–43. doi:10.1175/2007jpo3671.1.
- Capet, X., McWilliams, J.C., Molemaker, M.J., Shchepetkin, A.F., 2008c. Mesoscale to submesoscale transition in the California current system. part ii: Frontal processes. *J. Phys. Oceanogr.* 38 (1), 44–64. doi:10.1175/2007jpo3672.1.
- Capet, X., McWilliams, J.C., Molemaker, M.J., Shchepetkin, A.F., 2008d. Mesoscale to submesoscale transition in the California current system. part iii: Energy balance and flux. *J. Phys. Oceanogr.* 38 (10), 2256–2269. doi:10.1175/2008jpo3810.1.
- Charney, J.G., 1947. The dynamics of long waves in a baroclinic westerly current. *J. Meteorol.* 4 (5), 136–162.
- Demange, J., Debreu, L., Marchesiello, P., Lemarié, F., Blayo, E., 2014. On the use of a Depth-Dependent Barotropic Mode in Ocean Models: Impact on the stability of the Coupled Barotropic/Baroclinic System. Technical Report RR-8589. INRIA.
- Dukowicz, J.K., 2006. Structure of the barotropic mode in layered ocean models. *Ocean Modell.* 11 (1–2), 49–68.
- Dukowicz, J.K., Smith, R.D., 1994. Implicit free-surface method for the Bryan-Cox-Semtner ocean model. *J. Geophys. Res.* 99 (C4), 7991–8014. doi:10.1029/93JC03455.
- Durran, D.R., 1991. The 3rd-order Adams-Bashforth method - an attractive alternative to leapfrog time differencing. *Mon. Weather Rev.* 119 (3), 702–720. doi:10.1175/1520-0493(1991)119<0702:ttoabm>2.0.co;2.
- Durran, D.R., 2010. Numerical Methods for Fluid Dynamics: With Applications to Geophysics. Springer. Vol. 32 of Texts in Applied Mathematics.
- Frisch, U., Kurien, S., Pandit, R., Pauls, W., Ray, S., Wirth, A., Zhu, J., 2008. Hyperviscosity, galerkin truncation, and bottlenecks in turbulence. *Phys. Rev. Lett.* 101 (14).
- Griffies, S.M., Pacanowski, R.C., Hallberg, R.W., 2000. Spurious diapycnal mixing associated with advection in a z-coordinate ocean model. *Mon. Weather Rev.* 128, 538–563.
- Higdon, R.L., de Szoeko, R.A., 1997. Barotropic-baroclinic time splitting for ocean circulation modeling. *J. Comput. Phys.* 135 (1), 30–53.
- Holland, W.R., Chow, J.C., Bryan, F.O., 1998. Application of a third-order upwind scheme in the NCAR ocean model. *J. Clim.* 11 (6), 1487–1493. doi:10.1175/1520-0442(1998)011<1487:AOATOU>2.0.CO;2.
- Jiang, G.-S., Shu, C.-W., 1996. Efficient implementation of weighted (ENO) schemes. *J. Comput. Phys.* 126 (1), 202–228.
- Jouanno, J., Capet, X., Madec, G., Roulet, G., Klein, P., Masson, S., 2015. Dissipation of the energy imparted by mid-latitude storms in the southern ocean. *J. Phys. Oceanogr.* Submitted.
- Kent, J., Whitehead, J.P., Jablonowski, C., Rood, R.B., 2014. Determining the effective resolution of advection schemes. part i: Dispersion analysis. *J. Comput. Phys.* 278, 485–496.
- Klein, P., Hua, B.L., Lapeyre, G., Capet, X., Le Gentil, S., Sasaki, H., 2008. Upper ocean turbulence from high-resolution 3d simulations. *J. Phys. Oceanogr.* 38 (8). doi:10.1175/2007jpo3773.1.
- Leclair, M., Madec, G., 2009. A conservative leapfrog time stepping method. *Ocean Modell.* 30 (23), 88–94. http://dx.doi.org/10.1016/j.ocemod.2009.06.006.
- Lemarié, F., Debreu, L., Madec, G., Demange, J., Molines, J., Honnorat, M., 2015. Stability constraints for oceanic numerical models: implications for the formulation of time and space discretizations. *Ocean Modell.* 92, 124–148.
- Lemarié, F., Debreu, L., Shchepetkin, A.F., McWilliams, J.C., 2012. On the stability and accuracy of the harmonic and biharmonic isoneutral mixing operators in ocean models. *Ocean Modell.* 52–53, 9–35. doi:10.1016/j.ocemod.2012.04.007.
- Madec, G., 2008. NEMO Reference Manual, Ocean Dynamics Component: NEMO-OPA. Preliminary Version. Technical Report 27. Institut Pierre-Simon Laplace.
- Marchesiello, P., Capet, X., Menkes, C., Kennan, S.C., 2011. Submesoscale dynamics in tropical instability waves. *Ocean Modell.* 39 (1–2), 31–46. doi:10.1016/j.ocemod.2011.04.011.
- Marchesiello, P., Debreu, L., Couvelard, X., 2009. Spurious diapycnal mixing in terrain-following coordinate models: The problem and a solution. *Ocean Modell.* 26 (3–4), 156–169. doi:10.1016/j.ocemod.2008.09.004.
- Marsaleix, P., Auclair, F., Duhaut, T., Estournel, C., Nguyen, C., Ulses, C., 2012. Alternatives to the Robert-Asselin filter. *Ocean Modell.* 41 (0), 53–66.
- McWilliams, J.C., Chow, J.H.S., 1981. Equilibrium geostrophic turbulence: I. A reference solution in a beta-plane channel. *J. Phys. Oceanogr.* 11, 921–949.
- Molemaker, M.J., McWilliams, J.C., Capet, X., 2010. Balanced and unbalanced routes to dissipation in an equilibrated eddy flow. *J. Fluid Mech.* 654, 35–63. doi:10.1017/S0022112009993272.
- Orszag, S.A., 1971. Numerical simulation of incompressible flows within simple boundaries: accuracy. *J. Fluid Mech.* 49, 75–112. doi:10.1017/S0022112071001940.
- Redi, M.H., 1982. Oceanic isopycnal mixing by coordinate rotation. *J. Phys. Oceanogr.* 12 (1154–1154).
- Roberts, M., Marshall, D., 1998. Do we require adiabatic dissipation schemes in eddy-resolving ocean models? *J. Phys. Oceanogr.* 28, 2050–2063.
- Roulet, G., McWilliams, J.C., Capet, X., Molemaker, M.J., 2012. Properties of steady geostrophic turbulence with isopycnal outcropping. *J. Phys. Oceanogr.* 42 (1), 18–38. doi:10.1175/jpo-d-11-09.1.
- Sanderson, B.G., 1998. Order and resolution for computational ocean dynamics. *J. Phys. Oceanogr.* 28 (6), 1271–1286.
- Shchepetkin, A.F., McWilliams, J.C., 1998. Quasi-monotone advection schemes based on explicit locally adaptive dissipation. *Mon. Weather Rev.* 126 (6), 1541–1580. doi:10.1175/1520-0493(1998)126<1541:qmasbo>2.0.co;2.
- Shchepetkin, A.F., McWilliams, J.C., 2005. The regional oceanic modeling system (roms): a split-explicit, free-surface, topography-following-coordinate oceanic model. *Ocean Modell.* 9 (4), 347–404. doi:10.1016/j.ocemod.2004.08.002.
- Shchepetkin, A.F., McWilliams, J.C., 2009. Computational kernel algorithms for fine-scale, multiprocess, longtime oceanic simulations. In: Ciarlet, P. (Ed.), *Handbook of Numerical Analysis*. In: *Handbook of Numerical Analysis*, vol. 14. Elsevier, pp. 121–183.
- Shchepetkin, A.F., McWilliams, J.C., 2011. Accurate Boussinesq oceanic modeling with a practical, “stiffened” equation of state. *Ocean Modell.* 38 (1–2), 41–70. doi:10.1016/j.ocemod.2011.01.010.
- Skamarock, W.C., 2004. Evaluating mesoscale NWP models using kinetic energy spectra. *Mon. Weather Rev.* 132 (12), 3019–3032. doi:10.1175/mwr2830.1.
- Webb, D.J., de Cuevas, B.A., Richmond, C.S., 1998. Improved advection schemes for ocean models. *J. Atmos. Ocean. Technol.* 15 (5), 1171–1187.
- Zalesak, S.T., 1979. Fully multidimensional flux-corrected transport algorithms for fluids. *J. Comp. Phys.* 31 (3), 335–362.